Spin crossover supramolecular coordination compounds: design, synthesis and properties

Mohanad D .Darawsheh

Contents

CHAPTER 3: Spin Crossover in Iron (II) Dinuclear Triple-Stranded Helicates

3.1 Introduction

In chapter 1, some examples of dinuclear triple stranded helicates that exhibit SCO was discussed in detail. One of the interesting features of such helicates is the presence of cavity that could encapsulate small anions that could tune the SCO behavior. The presence of free functional group like N-H directed inside the cavity of the helicate can help to encapsulate hydrogen donor accepters. The pyrazolyl-pyridine moiety in ligand H_2L4 (Figure 3.1) offer such N-H groups in addition to the aromatic nitrogen donor properties that give the suitable environment for the SCO to occur. In chapter 2, the ability of this ligand to form triple stranded helicates with Co(II) and Ni(II) which encapsulate Cl^- in was discussed. The Cl^- encapsulation is stabilized with six hydrogen bonding afforded by the N-H groups. In this chapter, [Fe$_2$] triple stranded helicates using H_2L4 are discussed that encapsulate Cl^- or Br^- anions in their cavity. The nature of the anion affects the SCO temperature through affecting the ligand field around the metal ions. Changing the solvents or the outer anions affected also the SCO of the Fe(II) centers. Thus the three possible magnetic states, [HS-HS], [HS-LS] and [LS-LS] may be observed and stabilized over larger temperatures ranges, by playing with chemical variables. Moreover, some of the above magnetic states can be accessed also as meta-stable, using light irradiation.
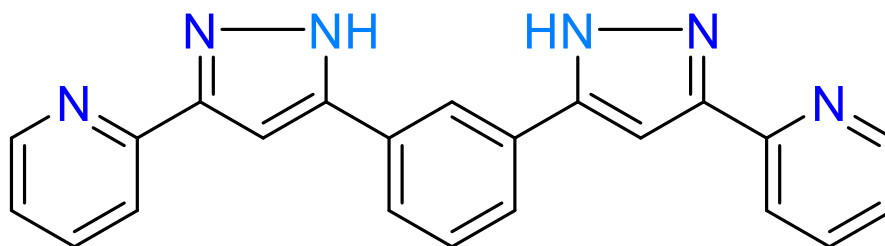
Figure 3.1: 1,3-bis(3-(pyridin-2-yl)-1H-pyrazol-5-yl)benzene (H$_2$L4).

3.2 Synthesis and Crystal Structure of Cl⊂[Fe$_2$(H$_2$L4)$_3$]Cl(PF$_6$)$_2$·5.7CH$_3$OH (1)

Complex **1** was prepared by reacting H$_2$L4 with FeCl$_2$·4H$_2$O (3:2 stoichiometry) in CH$_3$OH at room temperature for 45 minutes. The resulting red solution was treated with

two equivalents of NBu$_4$PF$_6$. The compound was isolated as red single crystals by slow diffusion of diethyl ether into the methanolic solution after a few days.
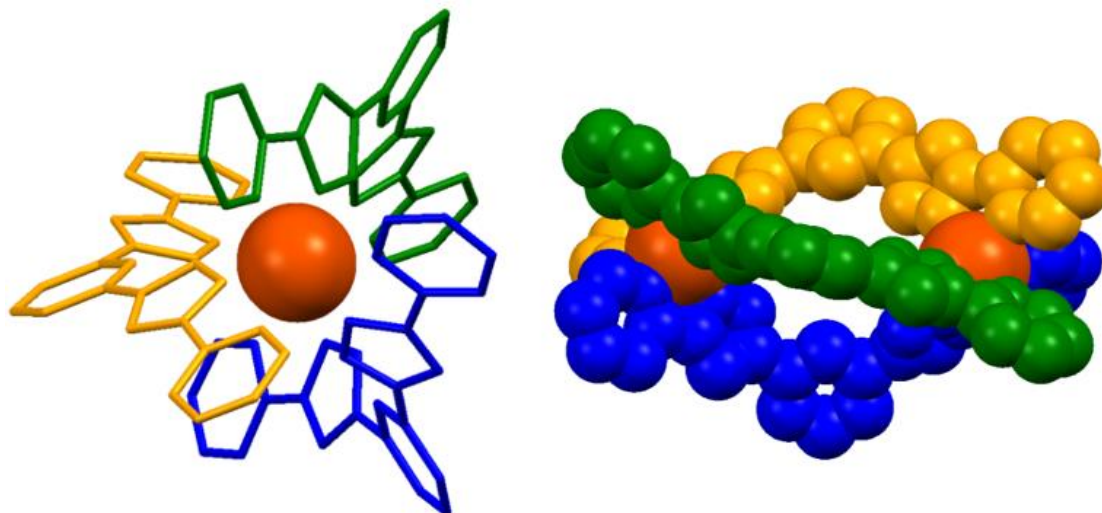
Figure 3.2: Left) Representation of the S-pseudo shape (front view) of the ligand around the dinuclear Fe$_2$ axis in **1**. Fe shown as orange ball and the three ligands have different colors. Fe-N bond is not shown. Right) triple stranded helicate in **1** represented by space filling mode with the central guest omitted for clarity. The ligands twist in S-shape and maintain the same stereochemistry around both iron centers (The one shown is $\Delta\Delta(P)$ right handed enantiomer).

Compound **1** crystallizes in the tetragonal non-centrosymmetric space group *I4$_1$cd* (*Z*=16). Crystallographic data and selected structural parameters at 100 K are shown in Tables 3.1 and 3.2. The asymmetric unit consists of a cationic $\{Cl \subset [Fe_2(H_2L4)_3]\}^{3+}$ encapsulating helicate, one Cl$^-$ and two PF$_6^-$ counterions in addition to five full MeOH molecules and one with 70 % partial occupancy. One of the PF$_6^-$ ions and three of the methanol molecules exhibit disorder over two positions. Three H$_2$L4 ligands adopt a pesudo-S shape (Figure 3.2) to offer the suitable helical surrounding around the principal axis defined by the two iron centers. In such a way every Fe(II) center exhibit a pseudo-octahedral coordination environment. The resulting helicate has *D$_3$*-symmetry.The *C3* axis is coincident with the Fe⋯Fe helical axis while three *C$_2$* axes are perpendicular to the latter. The *C2*-symmetry is supported by ligand which itself has this symmetry.

The S-shape of the ligand is achieved through the twisting around the C-C bond between the central phenylene and the pyrazole groups. This twisting is not identical for

the three ligands; one of them, which forms hydrogen bonds with the outer Cl⁻ ion (green ligand in Figure 3.3) exhibit similar twisting angles (44.12º and 39.15º, these being the angles between the two planes defined by the central phenylene group and the pyrazolyl group) in the both sides of the ligand. On the other hand, both remaining ligands show asymmetric twisting, with one angle larger than the other (average of related angles of 37.30 and 17.83º, respectively). This may rise from the varying hydrogen bonds in which the different ligands are engaged. A different behavior was observed in compound **3**, where the three ligands show similar twisting angles since they are not interacting with outer Cl⁻ ions (see section 3.7). The pyrazolyl-pyridine units in all ligands are approximately planar with torsion angles of less than 6º.
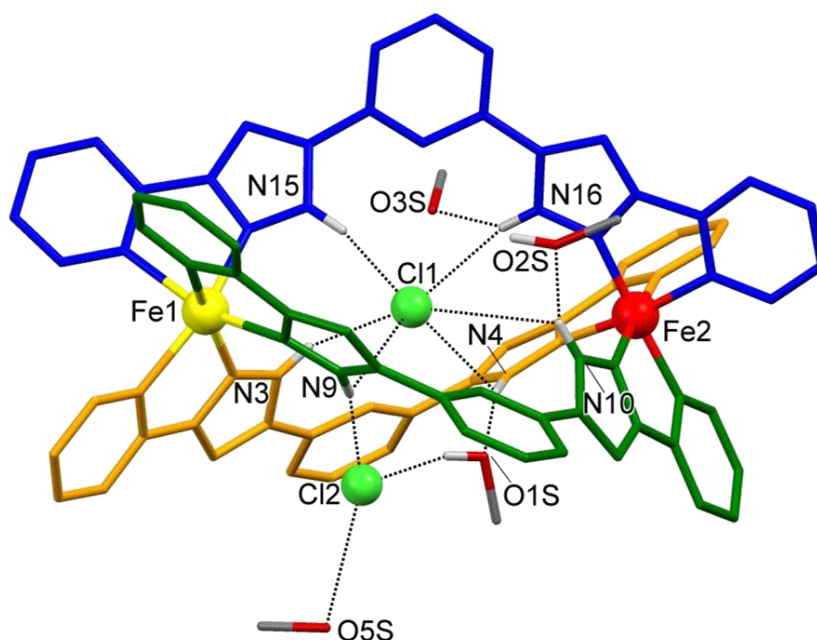
Figure 3.3: Molecular representation of $\{Cl \subset [Fe_2(H_2L4)_3]Cl\}^{2+}$ cation in **1** showing the hydrogen bonding between the NH groups and the two Cl⁻ counterions and the MeOH molecules. PF_6^- ions and two MeOH molecules are omitted for clarity. Only the hydrogen atoms on the pyrazole nitrogen atoms are shown. Only metals and heteroatoms involved in hydrogen bonding are labeled. HS and LS Fe(II) shown in yellow and red, respectively.

The two metal ions of each discrete helicate within the lattice of **1** have the same chirality. Thus each complex is either *ΔΔ(P)* or *ΛΛ(M)* leading to a racemic mixture of the two enantiomers in the crystal (Figure 3.2 represents the *ΔΔ(P)*, right handed enantiomer).

Both iron centers are separated by an intra-helical Fe⋯Fe distance of 9.731 Å. The helical length, defined by the distance between the centroids of the external carbon of the pyridyl groups of each side is, 15.803 Å. The radius of the helical cavity is around 3.534 Å. It is defined as the average distance between the H atom of the internal CH group in the phenylene unit of each ligand and the centroid of the three CH groups. The volume of the cavity is around 28 Å^3 as calculated using Swiss-Pdb Viewer 4.1.
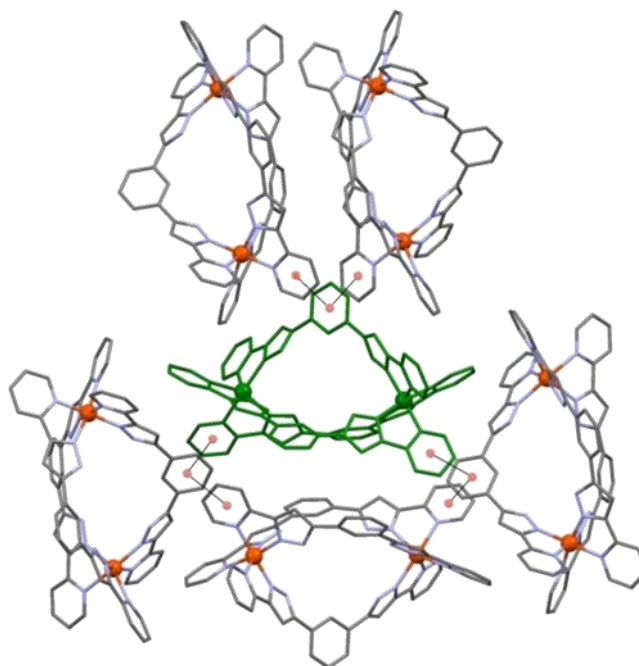
Figure 3.4: Representation of the interaction of a central helicate (green) of **1** and the surrounding first-equivalent neighbors, emphasizing the π-π interactions formed between them (Centroid to centroid distance is 3.766 or 4.133 Å). The C-H⋯π interactions are not shown. The same packing feature was observed in Br analogous (compound **2**) where π-π (Centroid to centroid) interactions is 3.760 and 4.249 Å.

One chloride ion (Cl1) is included inside the helical cavity and participates in six hydrogen bonds with the N-H groups of the pyrazolyl moieties. Two of these hydrogen bonds in one side of the helicate are much stronger than the others [N3-H⋯Cl1 = 2.426 and N15-H⋯Cl1 = 2.346 Å] (Table 3.3). This makes the Cl$^-$ to be closer to Fe1 (Fe1⋯Cl1 = 4.698 Å, Fe2⋯Cl1 = 5.038 Å) by 0.34 Å (Figure 3.3). The second chloride ion (Cl2) is located out of the cavity, closer to Fe1 and participating of a strong hydrogen bond with one NH group [N9-H⋯Cl2 = 2.269 Å]. The same chloride ion

forms also hydrogen bonds with two methanol molecules [O1S-H···Cl2 = 2.282 Å and O5S···Cl2 = 3.090 Å].
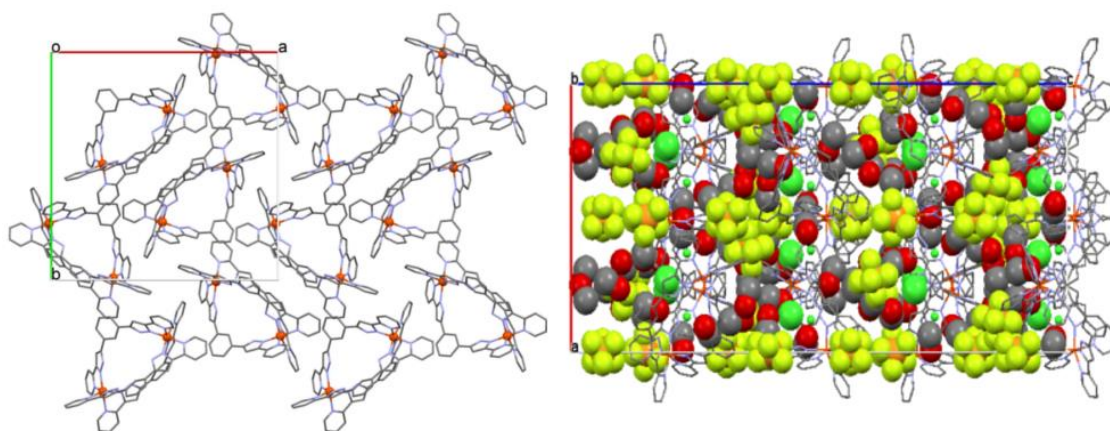
Figure 3.5: Left) Representation of a sheet of $[Fe_2(H_2L)_3]^{4+}$ helicates along the *ab* plane. Right) Packing diagram of compound **1** down the crystallographic *b* axis, emphasizing the alternation of "hydrophobic sheets" containing the largely organic $\{Cl{\subset}[Fe_2(H_2L)_3]\}^{3+}$ moieties (represented as capped sticks) and "hydrophilic layers" including external counter-ions and polar solvent molecules (represented in the space filling mode). The encapsulated Cl^- ions are represented as smaller balls. Hydrogen atoms are not shown.

On the other side of the helicate, near Fe2, three molecules of methanol participate of strong hydrogen bonds with three N-H groups [N4-H···O1S = 1.862, N10-H···O2S = 1.946 and N16-H···O3S = 2.354 Å]. One of these solvent molecules are engaged also with hydrogen bonds with the outer chloride ion [O1S-H···Cl2 = 2.282 Å]. In contrast, the PF_6^- ions do not participate in any strong interactions with the helicate.

All of these factors cause a different environment around the two crystallographically unique iron(II) centers, leading to different magnetic properties resulting from different spin configurations at 100 K, as indicated by different $(Fe-N)_{avg}$ distances around both centers. The Fe-N distances including the pyridine nitrogen atoms are longer than those belonging to the pyrazole ring. For Fe1, average distances of 2.143 Å and 2.234 Å were found for $Fe1-N_{pyridine}$ and $Fe1-N_{pyrazole}$, respectively. This indicates a high-spin configuration since $(Fe1-N)_{avg}$ equals 2.188 Å. On the other side, $Fe2-N_{pyridine}$ and $Fe2-N_{pyrazole}$ are shorter (1.958 and 2.000 Å, respectively) indicating a low-spin Fe(II) center $[(Fe2-N)_{avg} = 1.978$ Å]. These HS-LS mixed spin states underscore the effect of different intermolecular hydrogen bonding interactions on stabilizing the HS or LS state

of these centers. Hydrogen bonding of the type O···H-N stabilizes the low-spin state in Fe2 whereas the Cl···H-N type hydrogen bonds stabilize the high spin state in Fe1.

The packing in **1** describes two types of layer. The first is a hydrophobic layer made by sheets of $\{Cl \subset [Fe_2(H_2L4)_3]\}^{3+}$ species. Every helicate in the sheet is connected with five other neighbors through $\pi-\pi$ and C-H···π interactions *via* the aromatic rings, as seen in Figure 3.4 and Figure 3.5. Centroid to centroid distances of the $\pi-\pi$ interactions are 3.766 or 4.133 Å. The second layer is hydrophilic and contains the external Cl⁻ and the PF₆⁻ ions as well as the MeOH molecules (Figure 3.5). The two layers are parallel and alternative. This organization way allows the exchange of some solvent molecules with the environment while maintaining the crystallinity as suggested by the structure of the water solvate complex **1a** (see section 3.4). The ambient water can indeed exchange with MeOH through the hydrophilic layer, keeping the hydrophobic layer with the same organization.
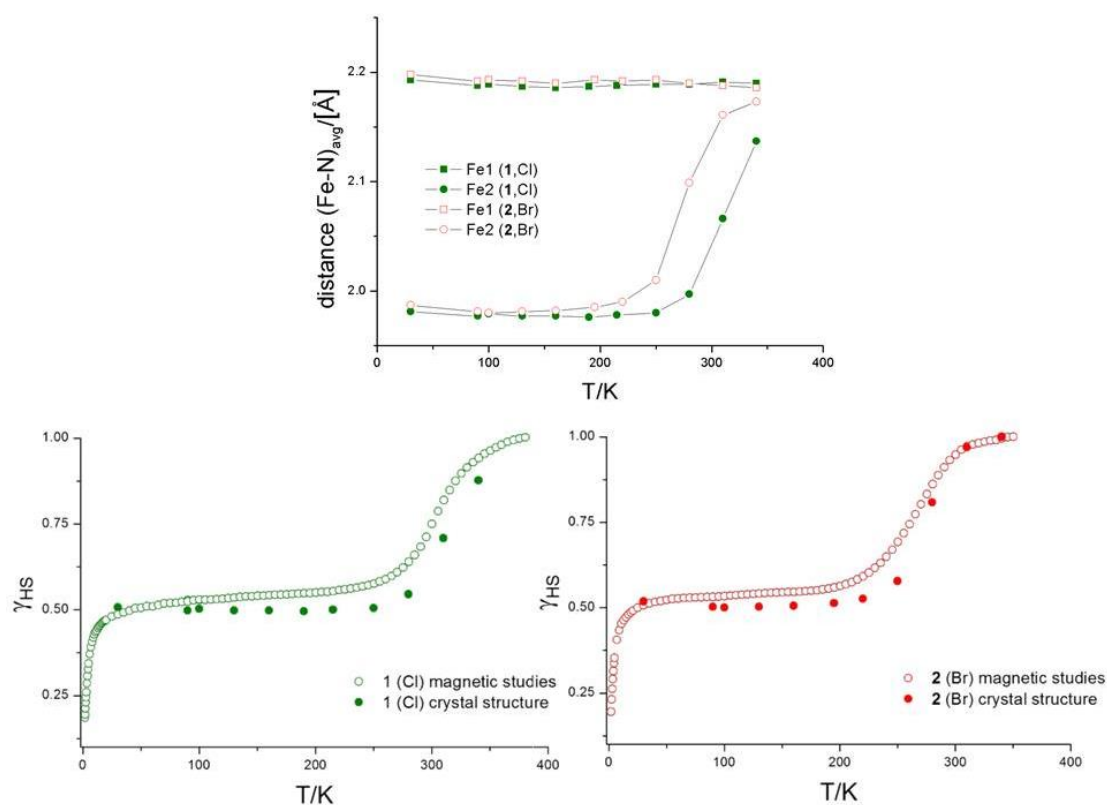
Figure 3.6: Top) Temperature dependence of $d_{(Fe-N)avg}$ for compounds **1** and **2** drawn for both Fe(II) centers. Botton) γ_{HS} vs temperature as driven from magnetic and crystal structure studies, $\gamma_{HS} = 0.5 + \{[\ d^{T}_{(Fe2-N)avg} - d^{LS}_{(Fe2-N)avg}] / [d^{HS}_{(Fe2-N)avg} - d^{LS}_{(Fe2-N)avg}]\}/2$ for compounds **1** (right) and **2** (left) {see text for details}.

As the two iron centers have different spin configurations, variable temperature crystallographic studies were conducted at eleven different temperatures, namely 30, 90, 100, 130, 160, 190, 215, 250, 280, 310 and 340 K, to investigate the variations of the magnetic state of these iron centers (Tables 3.1 and 3.2). The magnetic state of Fe1 remains HS in all studied range; Down to 30 K, Fe1-N_{avg} (2.193Å) is the same as seen at 340 K and corresponds to Fe(II) center in the HS state. This is not the case for Fe1, which exhibits a change from the LS state at temperatures lower than 280 K [(Fe2-N)$_{avg}$ = 1.997 Å] to the HS state at higher temperatures [(Fe2-N)$_{avg}$ = 2.137Å at 340 K]. The value increases by 0.16 Å, which corresponds to 88% conversion to HS state at 340 K, in agreement with magnetic studies (see Figure 3.6).

The evolution of (Fe2-N)$_{avg}$ with temperature indicates a gradual spin crossover (Figure 3.6) starting around 250 K while the (Fe1-N)$_{avg}$ remains constant at all temperatures. The molar HS fraction in **1** was derived from the structural data and calculated using this formula:

$$\gamma_{HS} = 0.5 + \{[d^T_{(Fe2-N)avg} - d^{LS}_{(Fe2-N)avg}]/[d^{HS}_{(Fe2-N)avg} - d^{LS}_{(Fe2-N)avg}]\}/2$$

Where d^T, d^{LS} and d^{HS} are the (Fe2-N)$_{avg}$ distances at a given temperature, of the full LS and full HS Fe(II), respectively. The number 0.5 represent the HS fraction for Fe1 since it has HS configuration at all temperatures. Plots of the molar high spin fraction *vs*. temperature derived from the structural data and that derived from the magnetic studies (see below) are shown in Figure 3.6. The two measurements are consistent and indicate the SCO behavior for Fe2 center. The characteristic temperature ($T_{1/2}$) at which 50% of HS⇔LS conversion in Fe2 has been accomplished is around 300 K. The completeness of SCO as indicated by the magnetic studies occurs higher than 340 K, which explains the 88 % of LS⇔HS conversion observed by the crystal structure at the highest measured temperature.

Another structural change associated to the SCO in Fe(II) is the distortion from the ideal octahedron. The HS state exhibits higher distortion than the LS state. The distortion parameter Σ and Θ is used in SCO compounds to indicate the deviation of a metal ion from an ideal octahedral symmetry (see chapter 1). A perfect octahedral complex gives $\Sigma = \Theta = 0$. High spin state complexes of a metal ion usually adopt a less regular (ideal) octahedral coordination geometry than their low spin counterparts[1] and therefore they exhibit higher Σ and Θ values (Table 3.2).
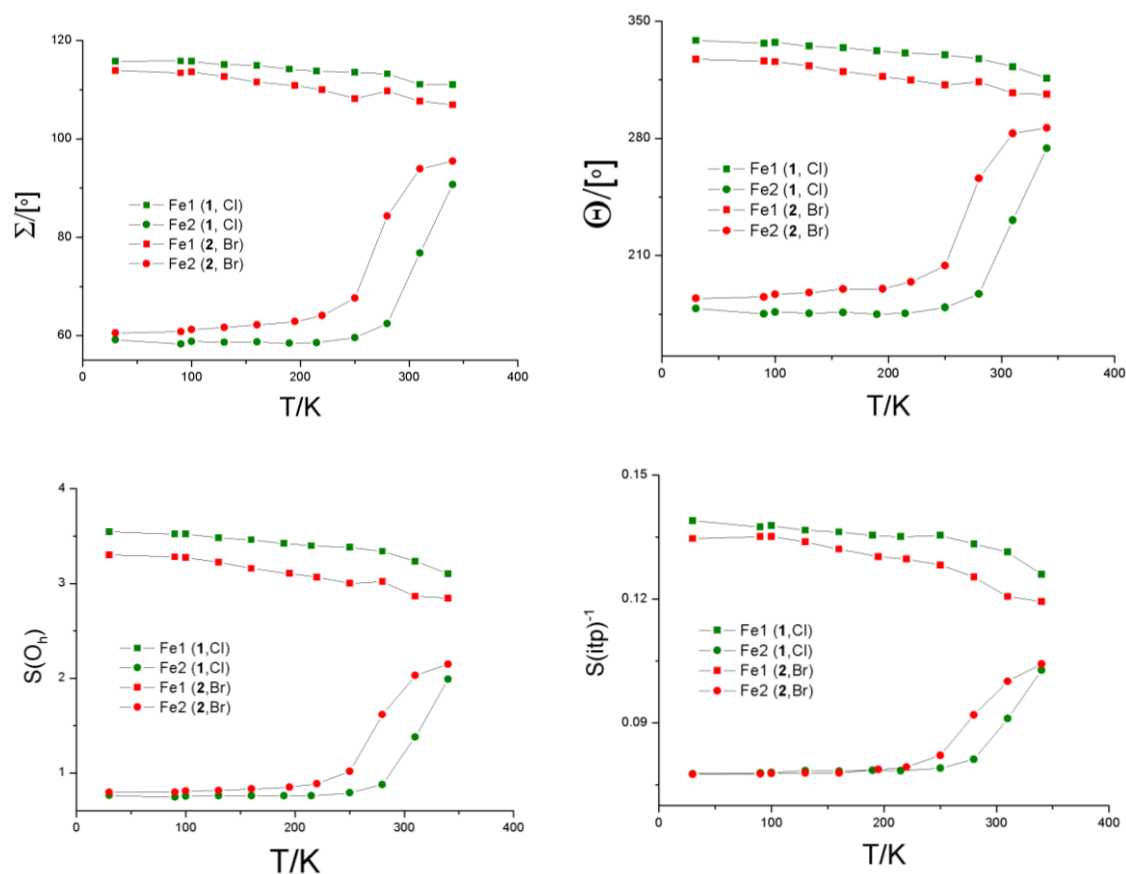
Figure 3.7: The octahedral distortion parameters Σ and Θ (top) and continuous symmetry measurements (bottom) of FeN$_6$ core relative to ideal octahedron (left) or ideal trigonal prism (Right, drawn as $S(itp)^{-1}$) vs. temperature for both distinct iron centers in compounds **1** and **2** , as determined from single crystal X-ray diffraction data.

Plots of the parameter Σ vs. temperature for both iron centers are shown in Figure 3.7. For Fe1, the value stays approximately constant around $\Sigma = 110°$ for all temperatures, while for Fe2, the value exhibits a dramatic change from 60° below 250 K to reach a value of 90° at 340 K as a result of the SCO. These results are consistent with the behavior observed in bulk magnetic studies (see below). The change of Θ parameter with temperature indicates the SCO in Fe2 which increases from around 175˚ at low temperatures to 274˚ at 340 K. The same parameter has similar values for Fe1 in all the temperature range since it is remain in the high spin.

Continuous symmetry measures were used to correlate the change in symmetry and shape of the metal coordination sphere with SCO behaviour[2]. The calculation of $S(O_h)$ and $S(itp)$, [which indicate the distance of FeN$_6$ to the octahedron and the trigonal prism core, respectively] were done for the distinct Fe1 and Fe2 centers at all studied

temperatures (Table 3.2). The closer to zero is the distance value the more ideal is the symmetry of the FeN_6 core ($S(O_h)$ = 0 ideal octahedron, $S(itp)$ = 0 ideal trigonal prism). For compound **1**, the values show that the LS configuration exhibits more ideal octahedral geometry and therefore lower $S(O_h)$ and higher $S(itp)$ values (Table 3.2).
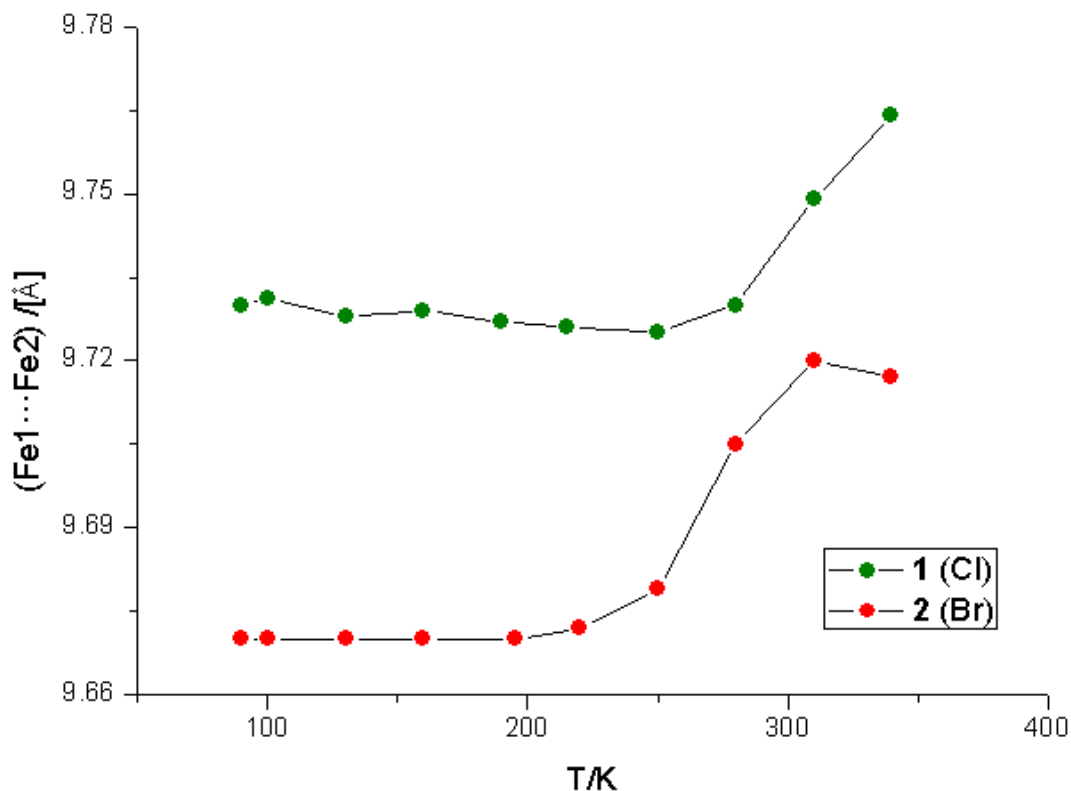
Figure 3.8: Inter-atomic distance Fe1⋯Fe2 within the helical structure in **1** and **2** as function of temperature.

Plotting these two continuous symmetry measures vs. temperature (Figure 3.7), beautifully shows a behavior analogous to the one seen with the $(Fe2-N)_{avg}$ plot and indicates a spin crossover starting from 250 K. Below this temperature, the $S(Oh)$ value for Fe2 is around 0.75 and as the temperature increases, the value increases importantly to reach 1.99 as a consequence of the distortion from the octahedron associated with the conversion from the LS to the HS state. This behavior is also supported by the change in $S(itp)$ value of Fe2 with temperature, which correlates also perfectly with the SCO behavior. The value remains around 12.5 at lower temperatures and over 250 K, it starts to decrease dramatically, down to 9.7 at 340 K. The $S(itp)$ value decreases as the FeN_6 core distorts from octahedral toward a trigonal prism geometry (Figure 3.7).

The $S(O_h)$ and $S(itp)$ values for Fe1 do not show any important change with the temperature. High $S(O_h)$ and low $S(itp)$ values for Fe1 (around 3.5 and 7.5, respectively) are expected since its coordination geometry exhibits high distortion as a result of its HS configuration at all temperatures. A slight decrease in Σ, Θ and $S(O_h)$ and a slight increase in $S(itp)$ was observed with the increase of temperature for this center. The two Fe(II) centers are connected through the helical structure and the dramatic change in the geometry around Fe2 as a result of the SCO could affect slightly the geometry around the HS center (Fe1). Moreover, Matouzenko et al. were demonstrated that in partial SCO (i.e. [HS-HS] → [HS-LS] transition) in binuclear compounds, the geometry of the HS iron center becomes more distorted as the geometry around LS site becomes more regular.[3] This agrees with the results in the current work since Fe1 exhibit stronger distortion as the temperature decrease.

The Fe1···Fe2 distance (Table 3.3) was also affected by the SCO behavior of Fe2. Figure 3.8 illustrates the change to the distance between both Fe(II) centers within the helical structure. In the range 30-250 K the distance remains within a narrow range (7.250-7.300 Å). Raising the temperature causes an important increase to 9.640 Å because of the Fe2-N distance elongation as a consequence of the SCO behavior.

Importantly, the $T_{1/2}$ value of the SCO deduced from all previous structural changes is close to 300 K, which is in agreement with the $T_{1/2}$ value observed in bulk magnetic studies.

The parameters of the intermolecular distances and hydrogen bonds between the helicate and Cl⁻ ions or MeOH molecules at different temperatures are shown in Table 3.3. As mentioned before, the main interactions include hydrogen bonds between N-H groups with either Cl⁻ anions or MeOH solvent molecules. These interactions show important changes in the range of temperatures of the SCO (250-340K). In general, increasing the temperature causes significant increases in these intermolecular interactions. N16-H···Cl1 is the only exception where the value decreases significantly with raising the temperature (Figure 3.3 and Table 3.3).

Table 3.1: Crystal data for compound **1**.

Formula	$C_{66}H_{48}Fe_2N_{18}$, 2(PF$_6$), 5.7(CH$_4$O), 2(Cl)										
FW (g mol^{-1})	1748.40										
Wavelength (Å)	0.77490										
Crystal system	Tetragonal										
Space group	$I4_1$cd										
Z	16										
T (K)	30(5)	90(2)	100(2)	130(2)	160(2)	190(2)	215(2)	250(2)	280(2)	310(2)	340(2)
a (Å)	24.373(2)	24.3518(9)	24.3653(9)	24.3963(8)	24.4454(9)	24.4897(10)	24.5239(9)	24.5807(9)	24.6268(9)	24.6863(9)	24.7420(10)
c (Å)	52.717(5)	52.692(2)	52.708(2)	52.761(2)	52.804(2)	52.826(2)	52.889(2)	52.972(2)	53.012(2)	53.048(2)	53.132(2)
V (Å^3)	31316(6)	31247(3)	31291(3)	31402(2)	31554(3)	31682(3)	31808(3)	32006(3)	32151(3)	32328(3)	32526(3)
ρ_{calcd} (g cm^{-3})	1.483	1.487	1.484	1.479	1.472	1.466	1.460	1.451	1.445	1.437	1.428
μ (mm^{-1})	0.693	0.695	0.694	0.715	0.688	0.685	0.682	0.678	0.675	0.671	0.667
Independent reflections	16134	11282	16056	11346	11406	11456	11495	11598	11664	11716	11783
restraints / parameters	197 / 1109	233 / 1109	251 / 1118	245 / 1118	257 / 1118	251 / 1118	251 / 1118	174 / 1048	180 / 1048	180 / 1048	187 / 1045
Goodness-of-fit on F^2	1.033	1.049	1.036	1.067	1.073	1.090	1.094	1.094	1.077	1.061	1.045
Final R_1/ wR_2 [$I>2\sigma(I)$]	0.0484 / 0.1265	0.0466 / 0.1243	0.0501 / 0.1322	0.0456 / 0.1202	0.0451 / 0.1185	0.0504 / 0.1314	0.0478 / 0.1240	0.0508 / 0.1318	0.0507 / 0.1314	0.0502 / 0.1291	0.0532 / 0.1378
Final R_1 / wR_2 [all data]	0.0585 / 0.1340	0.0512 / 0.1291	0.0584 / 0.1396	0.0519 / 0.1265	0.0527 / 0.1265	0.0595 / 0.1419	0.0590 / 0.1350	0.0642 / 0.1458	0.0654 / 0.1462	0.0642 / 0.1426	0.0728 / 0.1573
largest diff. peak and hole (e Å^3)	1.201 / −0.741	0.843 / −0.556	0.922 / −0.672	0.660 / −0.524	0.600 / −0.577	0.531 / −0.443	0.508 / −0.430	0.529 / −0.466	0.468 / −0.406	0.517 / −0.412	0.541 / −0.430

Table 3.2: Metal ligand Fe–N bond lengths (Å) and selected structural parameters in **1**.

T (K)	30(5)	90(2)	100(2)	130(2)	160(2)	190(2)	215(2)	250(2)	280(2)	310(2)	340(2)
Fe1–N14	2.136(5)	2.130(6)	2.131(5)	2.127(6)	2.128(6)	2.127(7)	2.132(7)	2.137(7)	2.140(7)	2.140(7)	2.146(8)
Fe1–N8	2.153(5)	2.154(6)	2.153(5)	2.154(6)	2.153(6)	2.147(6)	2.149(6)	2.146(6)	2.142(6)	2.140(6)	2.132(7)
Fe1–N2	2.153(5)	2.144(7)	2.145(5)	2.143(6)	2.138(6)	2.141(7)	2.139(7)	2.138(7)	2.140(7)	2.144(7)	2.137(8)
Fe1–N1	2.188(5)	2.191(6)	2.192(5)	2.197(6)	2.197(6)	2.197(6)	2.197(6)	2.202(6)	2.208(6)	2.207(6)	2.210(7)
Fe1–N13	2.254(5)	2.240(6)	2.246(5)	2.238(6)	2.238(6)	2.239(6)	2.240(6)	2.238(6)	2.237(6)	2.242(6)	2.246(7)
Fe1–N7	2.275(5)	2.267(6)	2.265(5)	2.263(6)	2.264(6)	2.269(7)	2.269(6)	2.270(7)	2.266(7)	2.273(7)	2.269(8)
Fe2–N17	1.960(5)	1.957(6)	1.959(5)	1.956(6)	1.959(6)	1.959(6)	1.962(6)	1.963(6)	1.977(7)	2.047(7)	2.115(9)
Fe2–N5	1.965(5)	1.954(6)	1.954(5)	1.952(6)	1.952(6)	1.953(6)	1.960(6)	1.958(6)	1.973(6)	2.032(6)	2.094(7)
Fe2–N11	1.965(5)	1.957(6)	1.961(5)	1.957(6)	1.956(6)	1.955(6)	1.959(6)	1.960(6)	1.981(7)	2.047(7)	2.121(8)
Fe2–N18	1.988(5)	1.982(6)	1.987(5)	1.986(6)	1.987(6)	1.986(6)	1.985(6)	1.985(6)	1.997(7)	2.065(7)	2.140(7)
Fe2–N6	2.002(5)	2.006(6)	2.006(5)	2.009(6)	2.007(6	2.004(6)	2.004(6)	2.010(6)	2.032(6)	2.114(6)	2.182(7)
Fe2–N12	2.008(5)	2.008(6)	2.009(5)	1.999(6)	1.999(6)	2.001(7)	2.000(6)	2.001(7)	2.020(7)	2.093(8)	2.168(8)
(Fe1-N)$_{avg}$	2.193	2.188	2.189	2.187	2.186	2.187	2.187	2.188	2.189	2.191	2.190
(Fe2-N)$_{avg}$	1.981	1.977	1.979	1.976	1.977	1.976	1.978	1.979	1.997	2.066	2.137
Σ (°)[a]	115.79/	115.85/	115.77/	115.12/	114.95/	114.20/	113.79/	113.56/	113.27/	111.08/	111.07/
	59.19	58.30	58.79	58.63	58.71	58.45	58.58	59.60	62.48	76.82	90.75
Θ (°)[a]	338.5/	336.8/	337.4/	335.2/	334.1/	332.3/	331.1/	329.9/	327.6/	322.9/	316.0/
	178.4	175.2	176.3	175.5	176.0	175.0	175.5	179.0	187.0	231.1	274.0
$S(Oh)$[a]	3.547/	3.522/	3.523	3.482/	3.461/	3.423/	3.398/	3.382/	3.340/	3.234/	3.102/
	0.762	0.745	0.755	0.756	0.759	0.759	0.756	0.788	0.875	1.377	1.989
$S(itp)$[a]	7.197/	7.272/	7.256/	7.315/	7.338	7.382/	7.401/	7.383/	7.498/	7.609/	7.940/
	12.868	12.844	12.815	12.750	12.765	12.740	12.754	12.651	12.316	10.985	9.728
V_{oct} (Å^3)[a]	13.259/	13.162/	13.182/	13.164/	13.160/	13.170/	13.190/	13.220/	13.220/	13.290/	13.290/
	10.210	10.161	10.186/	10.145	10.154	10.140	10.172	10.180	10.440	11.470	12.560

a) In Fe1/Fe2 form.

Table 3.3: Selected interatomic distances [Å] found in **1**.

Temperature (K)	30	90	100	130	160	190	215	250	280	310	340
Fe1···Fe2	9.750	9.730	9.731	9.728	9.729	9.727	9.726	9.725	9.730	9.749	9.764
Fe1···Cl1	4.707	4.699	4.698	4.701	4.704	4.705	4.710	4.714	4.718	4.729	4.771
Fe2···Cl1	5.048	5.036	5.038	5.032	5.031	5.027	5.022	5.017	5.018	5.027	5.001
N3-H···Cl1	2.430	2.427	2.426	2.432	2.435	2.438	2.450	2.458	2.482	2.514	2.582
N4-H···Cl1	3.155	3.131	3.133	3.130	3.139	3.138	3.147	3.142	3.143	3.138	3.123
N9-H···Cl1	3.107	3.114	3.110	3.126	3.132	3.152	3.149	3.156	3.175	3.208	3.272
N10-H···Cl1	3.303	3.299	3.295	3.293	3.287	3.282	3.275	3.274	3.281	3.321	3.261
N15-H···Cl1	2.348	2.344	2.346	2.354	2.352	2.351	2.368	2.377	2.406	2.443	2.490
N16-H···Cl1	2.904	2.902	2.905	2.901	2.889	2.879	2.879	2.872	2.854	2.798	2.713
N9-H···Cl2	2.286	2.271	2.269	2.265	2.267	2.259	2.272	2.274	2.272	2.259	2.251
N4-H···O1S	1.857	1.864	1.862	1.863	1.869	1.881	1.896	1.902	1.926	1.949	1.952
N10-H···O2S	1.956	1.943	1.946	1.952	1.948	1.949	1.961	1.964	1.976	2.009	2.140
N16-H···O3S	2.351	2.372	2.354	2.406	2.444	2.487	2.524	2.595	2.697	3.010	3.460
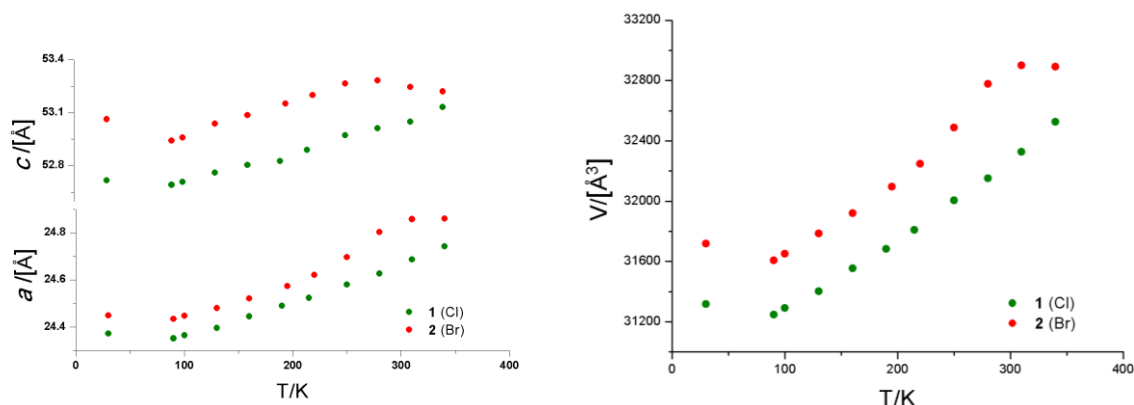
Figure 3.9: Plot of cell parameters change (Cell lengths *a* and *c* and cell volume) associated with temperature increasing in compounds **1** and **2**.

By contrast, plotting the cell parameters with temperature shows continuous gradual changes in the range 100-340K which can reasonably be ascribed to the thermal expansion of the lattice. Therefore, the SCO at Fe2 seen in the (Fe-N)$_{avg}$ does not induce any detectable variation of the cell parameters, which agrees with gradual character of the SCO as seen in the bulk magnetic measurements. This could be a consequence of the packing mode discussed before, which allows to accommodate the changes in Fe-N distances without any important changes in the unit cell. Moreover, the helical structure features void spaces and the twisting ability so as to accommodate these changes of the (Fe-N) distances.

3.3 Synthesis and Crystal Structure of Br⊂[Fe$_2$(H$_2$L4)$_3$]Br(PF$_6$)$_2$·4CH$_3$OH (2)

Complex **2** was prepared in similar manner to **1**, by reacting H$_2$L4 with FeBr$_2$ (3:2 stoichiometry) in CH$_3$OH, adding NBu$_4$PF$_6$ and then the slow diffusion of diethyl ether into the methanolic solution to get red single crystals after a few days. The structure of this compound is analogous to **1**, the main difference here being the two halide ions now Br$^-$ instead of Cl$^-$. Compound **2** crystallizes also in the tetragonal non-centrosymmetric space group *I4$_1$cd* (Z=16). Crystallographical data and selected structural parameters at 100 K are shown in Tables 3.4 and 3.5. The asymmetric unit now consists of the cationic {Br⊂[Fe$_2$(H$_2$L4)$_3$]}$^{3+}$ encapsulating helicate, one external Br$^-$ and two PF$_6^-$ counterions in addition to four MeOH molecules (Figure 3.10). The PF$_6^-$ ions exhibit disorder over two positions.
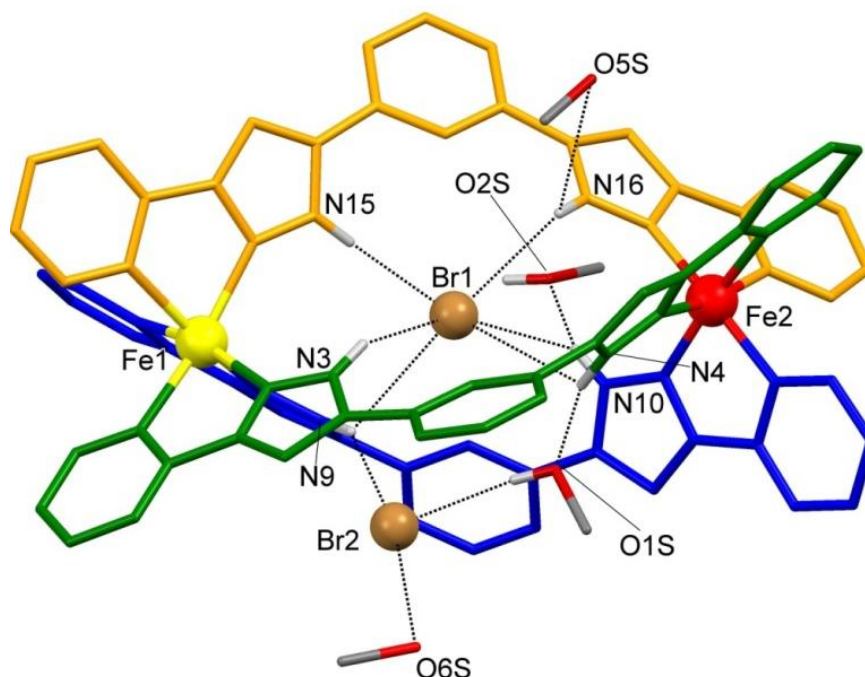
Figure 3.10: Molecular representation of {Br⊂[Fe$_2$(H$_2$L4)$_3$]}$^{3+}$ cation in **2** showing the hydrogen bonding between the NH groups and the two Br$^-$ counterions and the MeOH molecules. PF$_6^-$ ions and one MeOH molecule are omitted for clarity. Only hydrogen atoms on the pyrazole nitrogen atoms are shown. Only metals and heteroatoms involved in hydrogen bonding are labeled. HS and LS Fe(II) shown in yellow and red, respectively.

The chirality here again is maintained and a racemic mixture of the $\Delta\Delta$ (*P*) and the $\Lambda\Lambda$ (*M*) helicate is present in the lattice. The change to Br$^-$ does not affect any of the main structural features of the lattice. Br1 is encapsulated in the helical cavity and located closer to Fe1 by 0.094 Å [Fe1···Br1 = 4.789 and Fe2···Br1 = 4.883 Å] as a result of stronger hydrogen bonds with two of the N-H groups [N3-H···Br1 =2.594 Å and N15-H···Br1= 2.492 Å]. This difference in Fe···Br distances is much smaller than the one observed in **1**, which is 0.34 Å. The Intra-helical Fe1···Fe2 distance is now 9.670Å, which is also shorter than the one observed in **1** by 0.061 Å. However, the cavity volume is now 33 Å^3 which is slightly larger than the one observed in the Cl$^-$ analogue (28 Å^3) presumably to accommodate better the bigger bromide ion. Br2 is located out of the cavity and participates in a strong hydrogen bond with one N-H group [N9-H···Br = 2.474 Å]. The pyrazole groups near the Fe2 side exhibit strong hydrogen bonds with three MeOH molecules (Figure 3.10 and Table 3.6).

Again here, the electronic configurations of Fe1 and Fe2 at 100 K are different, (Fe1-N)$_{avg}$ = 2.193 and (Fe2-N)$_{avg}$ = 1.980 Å, as a consequence of the different hydrogen bonding with the NH of the pyrazolyl rings near them. The NH groups close to Fe1 are engaged in hydrogen bonds with bromide, while the NH groups near Fe2 establish hydrogen bonds mainly with MeOH solvent molecules (Figure 3.10).

The structure of **2** was determined at eleven different temperatures between 30 and 340 K (Tables 3.4 and 3.5). The plot of (Fe-N)$_{avg}$ *vs.* temperature indicate SCO behavior of Fe2 as in compound **1** (Figure 3.6). Below 220 K, (Fe2-N)$_{avg}$ is around 1.98 Å indicating a LS state. Heating causes a gradual increase of the value up to 2.17 Å at 340 K indicating a transition to the HS state. The (Fe1-N)$_{avg}$ value remains almost the same (2.19 Å) since this iron center is in the HS state over all the temperature range. The plot of HS mole fraction *vs.* temperature derived from structural data and magnetic studies is shown in Figure 3.6. Both plots are consistent and show a gradual SCO with $T_{1/2}$ around 270 K. The change in the halide from chloride to bromide caused less stabilization of the LS spin state as indicated by the down shift in $T_{1/2}$.

The change in the distortion parameters Σ and Θ with temperature for both iron centers are shown in Figure 3.7. The results indicate the SCO behavior in Fe2. The change occurs in the range of the SCO seen from the magnetic studies and reflects the distortion accompany this transition. The change in the distortion parameter ($\Delta\Sigma = 35°$, $\Delta\Theta = 101°$) in compound **2** as a result of SCO is similar to that occurred in **1** ($\Delta\Sigma = 30°$, $\Delta\Theta = 99°$). The Σ and Θ values of Fe1 does not exhibit any important variation, which expected since it HS at all temperatures. Continuous symmetry measurements (factors [$S(O_h)$ and $S(itp)$]) were performed for both Fe(II) centers at all temperatures (Figure 3.7). The $S(O_h)$ value for Fe2 is around 0.8 below 220 K. The value starts to increase importantly above 220 K, to reach 2.15 at 340 K. Moreover, the $S(itp)$ value decreases over the same range of temperatures from 12.82 at low temperatures to 9.52 at high temperatures. These values indicate the high distortion around Fe2 from octahedral geometry towards a trigonal prism as a result of the change in the spin state.

The $T_{1/2}$ value derived from the observed changes indicates that the SCO behavior is consistent with the one seen in the magnetic studies and the change in (Fe2-N)$_{avg}$. All curves of [Σ, $S(O_h)$ and $S(itp)$] vs temperature for **2** are shifted to lower temperature as

compared to compound **1**, which indicates a lower $T_{1/2}$ (around 40 K difference) for **2**, in agreement with the magnetic studies.

The change in the Fe1···Fe2 distance is analogous to **1**, also shifted to lower temperature (from 9.670 Å below 220 K to 9.670 Å at 340 K, Figure 3.8). Thus, all structural changes shown by **2** indicate a shift in $T_{1/2}$ by 30-40 K in comparison to what observed in **1**. Stronger hydrogen bonds in the Cl$^-$ analogue stabilize the LS state in the helicate with respect to the Br$^-$ analogue.

The cell parameters in **2** show a gradual increase in the range 100-280 K, which can be mainly ascribed again to thermal expansion of the lattice (Figure 3.9). There is however, what seems to be a stronger increase in the SCO range above 280 K which could be taken as a consequence of the SCO in Fe2, different from the behavior in **1**. However, this behavior still agrees with the gradual character of the SCO. The peculiar change above 310 K may be influenced by the onset of some lattice MeOH molecule loss at that temperature as seen through crystal structure measurements at 340 K.
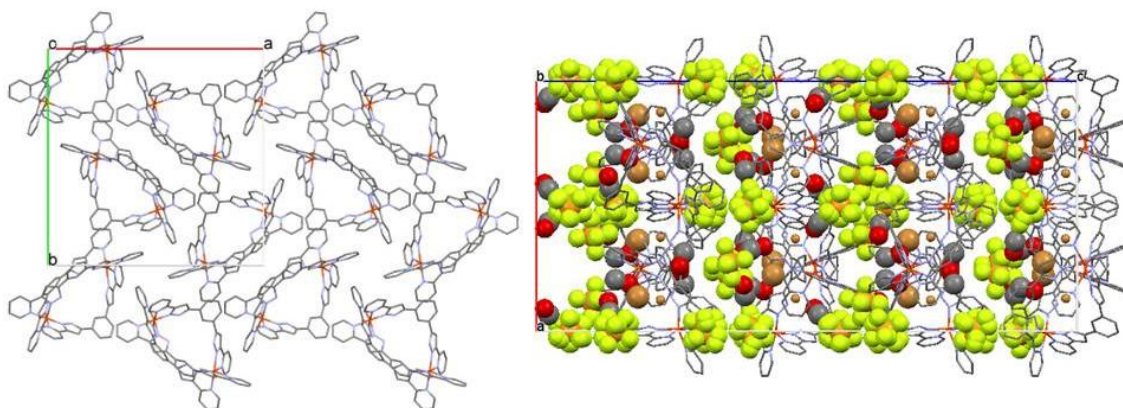
Figure 3.11: Left) Representation of a sheet of $[Fe_2(H_2L)_3]^{4+}$ helicates along the *ab* plane. Right) packing diagram of **2** down the crystallographic *b* axis, showing an alternative layers of "hydrophobic sheets" containing the largely organic $\{Br \subset [Fe_2(H_2L)_3]\}^{3+}$ moieties (represented as capped sticks) and "hydrophilic layers" including external counter-ions and polar solvent molecules (represented in the space filling mode). The encapsulated Br$^-$ ions are represented as small balls. Hydrogen atoms are not shown.

Moreover, intermolecular interactions between the helicate and bromide ions or methanol molecules are affected importantly by the SCO behavior as illustrated in Table 3.6. Over 220 K, most of these values increase significantly as a result of the structural change accompanying the SCO. The values at T = 340 K show different trends since

Table 3.4: Crystal data for compound **2**.

	30(5)	90(2)	100(2)	130(2)	160(2)	195(2)	220(2)	250(2)	280(2)	310(2)	340(2)
Formula	$C_{66}H_{48}Fe_2N_{18}$, 2(PF$_6$), 4(CH$_4$O), 2(Br)										$C_{66}H_{48}Fe_2N_{18}$, 2(F$_6$P), 3.4(CH$_4$O), 2(Br)
FW (g mol^{-1})	1782.85										1764.83
Wavelength (Å)	0.77490										
Crystal system	Tetragonal										
Space group	$I4_1cd$										
Z	16										
T (K)	30(5)	90(2)	100(2)	130(2)	160(2)	195(2)	220(2)	250(2)	280(2)	310(2)	340(2)
a (Å)	24.449(3)	24.4344(8)	24.4473(8)	24.4809(8)	24.5221(8)	24.5732(8)	24.6206(8)	24.6967(8)	24.8026(8)	24.8574(8)	24.8601(8)
c (Å)	53.063(6)	52.942(2)	52.959(2)	53.038(2)	53.085(2)	53.151(2)	53.200(2)	53.264(2)	53.282(2)	53.245(2)	53.220(2)
V (Å^3)	31719(9)	31608(2)	31652(2)	31786(2)	31922(2)	32095(2)	32248(2)	32487(2)	32777(2)	32900(2)	32891(2)
ρ_{calcd} (g cm^{-3})	1.494	1.499	1.497	1.490	1.484	1.476	1.469	1.458	1.445	1.440	1.426
μ (mm^{-1})	1.868	1.867	1.865	1.857	1.849	1.839	1.830	1.817	1.801	1.794	1.793
Independent reflections	16905	18194	17446	18303	18373	18463	17794	16008	15554	14515	12630
restraints / parameters	119 / 1065	119 / 1065	119 / 1065	119 / 1065	140 / 1065	146 / 1065	165 / 1065	165 / 1065	235 / 1043	263 / 1043	262 / 1035
Goodness-of-fit on F^2	1.064	1.058	1.066	1.063	1.065	1.054	1.059	1.078	1.076	1.092	1.090
Final R_1 / wR_2 [$I>2\sigma(I)$]	0.0492 / 0.1349	0.0530 / 0.1487	0.0519 / 0.1455	0.0522 / 0.1450	0.0519 / 0.1422	0.0518 / 0.1388	0.0533 / 0.1444	0.0579 / 0.1581	0.0565 / 0.1530	0.0556 / 0.1476	0.0598 / 0.1607
Final R_1 / wR_2 [all data]	0.0549 / 0.1398	0.0602 / 0.1548	0.0583 / 0.1512	0.0619 / 0.1536	0.0640 / 0.1529	0.0683 / 0.1532	0.0692 / 0.1585	0.0741 / 0.1725	0.0757 / 0.1704	0.0763 / 0.1682	0.0806 / 0.1847
largest diff. peak and hole (e Å^3)	2.729 / –0.458	2.753 / –0.677	2.634 / –0.626	2.169 / –0.658	1.942 / –0.654	1.296 / –0.671	1.223 / –0.648	0.993 / –0.658	0.856 / –0.650	0.766 / –0.657	0.689 / –0.727

Table 3.5: Metal ligand Fe–N bond lengths (Å) and some structural parameters in compound **2**.

| T (K)	30(5)	90(2)	100(2)	130(2)	160(2)	195(2)	220(2)	250(2)	280(2)	310(2)	340(2)
Fe1–N14	2.143(6)	2.133(6)	2.133(6)	2.138(6)	2.138(6)	2.139(6)	2.146(7)	2.151(8)	2.143(7)	2.155(7)	2.154(9)
Fe1–N2	2.154(6)	2.152(7)	2.153(6)	2.150(6)	2.143(6)	2.149(6)	2.140(6)	2.143(8)	2.143(7)	2.142(8)	2.141(9)
Fe1–N8	2.169(6)	2.163(6)	2.165(6)	2.164(5)	2.163(5)	2.164(5)	2.162(5)	2.167(7)	2.157(7)	2.145(7)	2.144(9)
Fe1–N1	2.205(6)	2.202(6)	2.204(6)	2.201(6)	2.198(6)	2.205(6)	2.206(6)	2.210(7)	2.202(7)	2.196(7)	2.189(9)
Fe1–N13	2.257(6)	2.248(6)	2.246(6)	2.241(6)	2.240(6)	2.244(6)	2.238(6)	2.235(7)	2.234(7)	2.241(7)	2.242(8)
Fe1–N7	2.262(6)	2.256(6)	2.258(6)	2.256(6)	2.256(6)	2.256(6)	2.257(6)	2.254(8)	2.258(7)	2.246(8)	2.248(9)
Fe2–N5	1.960(6)	1.949(6)	1.947(6)	1.949(6)	1.946(5)	1.957(5)	1.964(6)	1.984(7)	2.080(7)	2.128(7)	2.140(9)
Fe2–N11	1.964(6)	1.961(6)	1.954(6)	1.951(6)	1.951(5)	1.957(5)	1.951(6)	1.974(8	2.078(8)	2.138(7)	2.144(9)
Fe2–N17	1.974(6)	1.974(6)	1.977(6)	1.978(6)	1.980(6)	1.981(6)	1.987(7)	1.997(8)	2.080(8)	2.133(8)	2.143(10)
Fe2–N18	1.994(6)	1.992(7)	1.992(6)	1.996(6)	1.996(6)	1.991(6)	1.998(6)	2.009(9)	2.089(9)	2.167(8)	2.182(9)
Fe2–N12	2.013(6)	2.004(6)	2.001(6)	2.003(6)	2.003(6	2.005(6)	2.016(7)	2.045(9)	2.125(9)	2.197(8)	2.210(9)
Fe2–N6	2.014(6)	2.008(6)	2.007(6)	2.011(6)	2.014(6)	2.019(6)	2.021(6)	2.052(7)	2.140(7)	2.204(7)	2.219(8)
$(Fe1-N)_{avg}$	2.198	2.192	2.193	2.192	2.190	2.193	2.191	2.193	2.189	2.187	2.186
$(Fe2-N)_{avg}$	1.986	1.981	1.980	1.981	1.982	1.985	1.989	2.010	2.099	2.161	2.173
$\Sigma (°)^{a}$	113.92/	113.43/	113.63/	112.69/	111.56/	110.88/	109.98/	108.21/	109.76/	107.7/	106.94/
	60.54	60.81	61.22	61.63	62.20	62.83	64.07	67.64	84.30	93.91	95.51
$\Theta (°)^{a}$	327.3/	326.3/	325.8/	323.4/	319.9/	317.0/	314.9/	312.0/	313.8/	307.1/	306.3/
	184.5	185.2	186.9	187.8	190.0	190.1	194.2	204.0	256.1	283.0	286.2
$S(Oh)^{a}$	3.301/	3.280/	3.274/	3.224/	3.158/	3.105/	3.067/	3.001/	3.020/	2.865/	2.843/
	0.793	0.797	0.809	0.815	0.830	0.849	0.885	1.016	1.616	2.029	2.148
$S(itp)^{a}$	7.426/	7.400/	7.402/	7.471/	7.570/	7.676/	7.711/	7.796/	7.978/	8.290/	8.377/
	12.896	12.866	12.862	12.841	12.834	12.702	12.606	12.176	10.872	9.992	9.590
V_{oct} (Å^{3})^{a}	13..40/	13.30/	13.32/	13.29/	13.27/	13.34/	13.32/	13.37/	13.29/	13.28/	13.27/
	10.28	10.21	10.18	10.20	10.20	10.25	10.32	10.62	11.96	12.98	13.17

a) In Fe1/Fe2 form.

Table 3.6: Selected interatomic distances [Å] found in **2**.

Temperature (K)	30	90	100	130	160	195	220	250	280	310	340
Fe1···Fe2	9.689	9.670	9.670	9.670	9.670	9.670	9.672	9.672	9.679	9.705	9.717
Fe1···Br1	4.797	4.790	4.789	4.787	4.787	4.786	4.788	4.790	4.794	4.800	4.812
Fe2···Br1	4.895	4.883	4.883	4.885	4.885	4.886	4.887	4.892	4.915	4.923	4.909
N3-H···Br1	2.608	2.600	2.594	2.584	2.577	2.583	2.596	2.605	2.654	2.677	2.688
N4-H···Br1	3.121	3.115	3.123	3.131	3.127	3.134	3.149	3.138	3.137	3.134	3.124
N9-H···Br1	3.084	3.087	3.084	3.089	3.098	3.110	3.123	3.131	3.188	3.227	3.262
N10-H···Br1	3.169	3.168	3.175	3.156	3.144	3.147	3.143	3.160	3.196	3.250	3.162
N15-H···Br1	2.488	2.481	2.492	2.508	2.527	2.539	2.552	2.548	2.577	2.606	2.618
N16-H···Br1	2.775	2.771	2.773	2.792	2.804	2.798	2.881	2.795	2.793	2.787	2.784
N9-H···Br2	2.486	2.481	2.474	2.475	2.474	2.463	2.477	2.474	2.488	2.431	2.432
N4-H···O1S	1.837	1.840	1.835	1.837	1.841	1.849	1.860	1.886	1.942	1.962	2.017
N10-H···O2S	1.977	1.972	1.969	1.987	1.992	1.997	2.020	2.032	2.090	2.088	2.174

one methanol has been lost at high temperature as seen by single crystal structure measurements.

The packing in the lattice in **2** is similar to the one observed in compound **1**. The $\{Br \subset [Fe_2(H_2L)_3]\}^{3+}$ helicates are organized in sheets connected together with $\pi - \pi$ and C-H$\cdots\pi$ interactions of the aromatic rings as seen in the Cl⁻ analogue. Every helicate is surrounded by five close neighbors as seen in Figure 3.4. These sheets are parallel to hydrophilic layers containing the counter ions and the solvent molecules (Figure 3.11). Again here, this organization should allow the exchange of solvent molecules with the environment while maintaining the crystallinity as we will see with compound **2a** (water solvate analogous of compound **2**). Methanol molecules can escape through these layers allowing ambient water molecules to enter while the hydrophobic sheets are not affected.
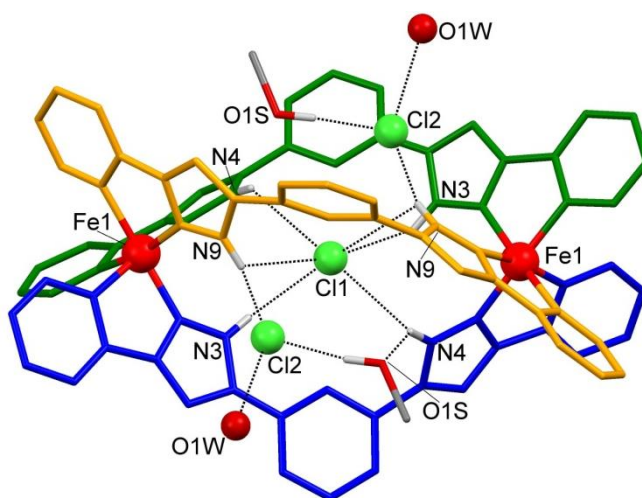
Figure 3.12: Molecular representation of $\{Cl \subset [Fe_2(H_2L4)_3)]Cl\}^{2+}$ in **1a** showing the disorder in Cl2, one molecule of water and one CH_3OH. The hydrogen bonding with N-H groups are shown. PF_6^- ions and two MeOH molecules are omitted for clarity. Only the hydrogen atoms on the pyrazole nitrogen atoms are shown. Only metals and heteroatoms involved in hydrogen bonding are labeled.

3.4   Crystal Structure of $Cl \subset [Fe_2(H_2L4)_3]Cl(PF_6)_2 \cdot 3CH_3OH \cdot 1H_2O$ (1a)

After exposing the crystals of **1** to air for five days, a slight change in color was observed while the crystallinity was presented. Indeed, it was possible to measure the crystal structure again to give a water solvate helicate, **1a.** Now the system is found in

the centrosymmetric tetragonal space group $I4_1acd$. Crystallographic data and structural parameters at 90 K are shown in Tables 3.7 and 3.8. The asymmetric unit consists of half helicate. The lattice solvents now are three molecules of CH_3OH and one molecule of water, as a result of the solvent exchange with the environment in a single-crystal to single-crystal (SCSC) manner. The alternative hydrophilic-hydrophopic-layers of the lattice packing mentioned before probably allow this solvent exchange without losing crystallinity. This exchange leads to important changes; the $\{Cl \subset [Fe_2(H_2L4)_3]\}^{3+}$ helicate are now symmetric and the two Fe centers are crystallographically identical. The encapsulated Cl^- is now in the center of the helicate with same distances to both Fe centers (Fe$\cdots$Cl1 = 4.838 Å). This increased symmetry is achieved because of the disorder over two positions (50% each) exhibited by the out-of-cavity Cl^- ion, one methanol molecule and one water molecule, both participating in hydrogen bonds with the same Cl2 ion. The disorder locates this ion near one or the other Fe(II) centers (Figure 3.12) resulting in two crystallographically identical Fe(II) ions. For each individual molecule of the solid, both Fe(II) centers need, however, to be necessarily different.

Selected intermolecular distances and interactions are shown in Table 3.9. The hydrogen bonding interaction N9-H$\cdots$Cl2 (2.055Å) is much stronger here than the one observed in compound **1** (2.271Å). Importantly, Cl2 now is disordered over two positions and the N9-H$\cdots$Cl2 hydrogen bond is close to both Fe(II) centers. The N-H$\cdots$Cl1 hydrogen bonds are now symmetrical around both Fe(II) centers for the encapsulated chloride and have an average value of 2.889 Å. This value is very close to the one observed in **1** (2.868 Å). The intrahelical Fe1$\cdots$Fe1 distance is 9.675 Å, shorter than the corresponding value in **1** by 0.055 Å. Cl2 is also involved in hydrogen bonds with a water molecule [Cl2$\cdots$O1W distance of 2.741Å] and a CH_3OH molecule [Cl2$\cdots$O1S distance of 3.000 Å]. In compound **1**, the same chloride is involved in hydrogen bonds with two CH_3OH molecules.

The packing organization of **1a** is similar to the one observed in **1**, consisting of sheets of $\{Cl \subset [Fe_2(H_2L4)_3]\}^{3+}$ connected through $\pi - \pi$ and C-H$\cdots\pi$ interactions involving the aromatic rings. Centroid to centroid $\pi - \pi$ distances here are the same as in **1** (4.133 or 3.759 Å) as seen in Figure 3.4. These sheets formed by helicate assemblies alternate with these formed by anions and the solvent molecules. Figure 3.13 illustrates the

dramatic effect of solvent exchange, causing a displacement of 50% of the Cl2 ions by approximately 9 Å, or a partial substitution with the encapsulated anion in going from one side of the helicate to the other.
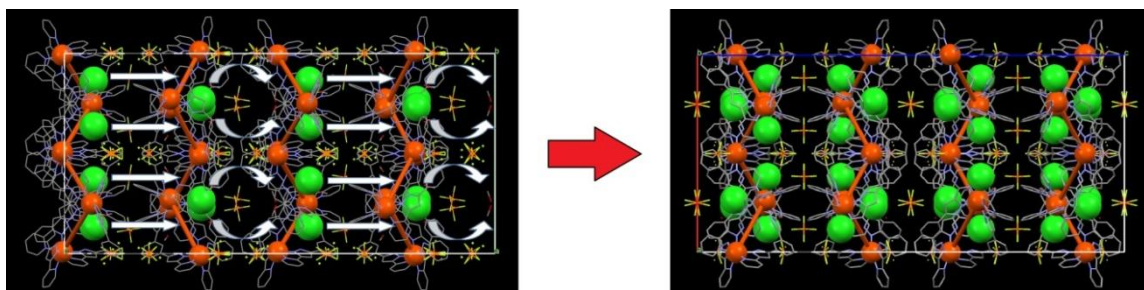
Figure 3.13: Representation of the unit cell of **1** and **1a**, emphasizing the displacement of 50% of the Cl$^-$ ions (represented in space filling format) that results from the MeOH exchange by H$_2$O. The Fe atoms of each helicate are represented as orange balls linked by rod of the same color. The remaining atoms are represented in wireframe format

The structure of **1a** was determined at 30, 90, 215 and 300 K (Table 3.7). The (Fe-N)$_{avg}$ values at 30 and 90 K indicate a LS configuration (1.982 and 1.983 Å, respectively). Heating causes an increase in this value ((Fe-N)$_{avg}$ = 2.157 Å at 300 K), indicating a conversion to the HS state (Figure 3.14). The Δ(Fe-N)$_{avg}$ indicates a 90 % conversion from [LS-LS] to [HS-HS] states of the dinuclear helicates, which is consistent with bulk magnetic susceptibility measurements (around 91% of conversion at 300 K). However, the structural data at 215 K does not allow a description of the LS-HS states distribution among the metals during the transition, which was observed in the bulk magnetic susceptibility measurements (see section 3.9) because at this temperature both metal centers are identical with (Fe-N)$_{avg}$ equal to 2.050 Å. This corresponds to the average value between [HS-HS] and [LS-LS] states. Taking into account that the disordered Cl2 and CH$_3$OH species are in one place at one time, the two Fe centers of each individual molecule must be different. The crystallographic equivalence of both iron centers is in fact a consequence of the averaging of all the disordered components. The necessary difference of both ions could thus not be proofed crystallographically, but bulk magnetic studies indicate this dissimilarity.
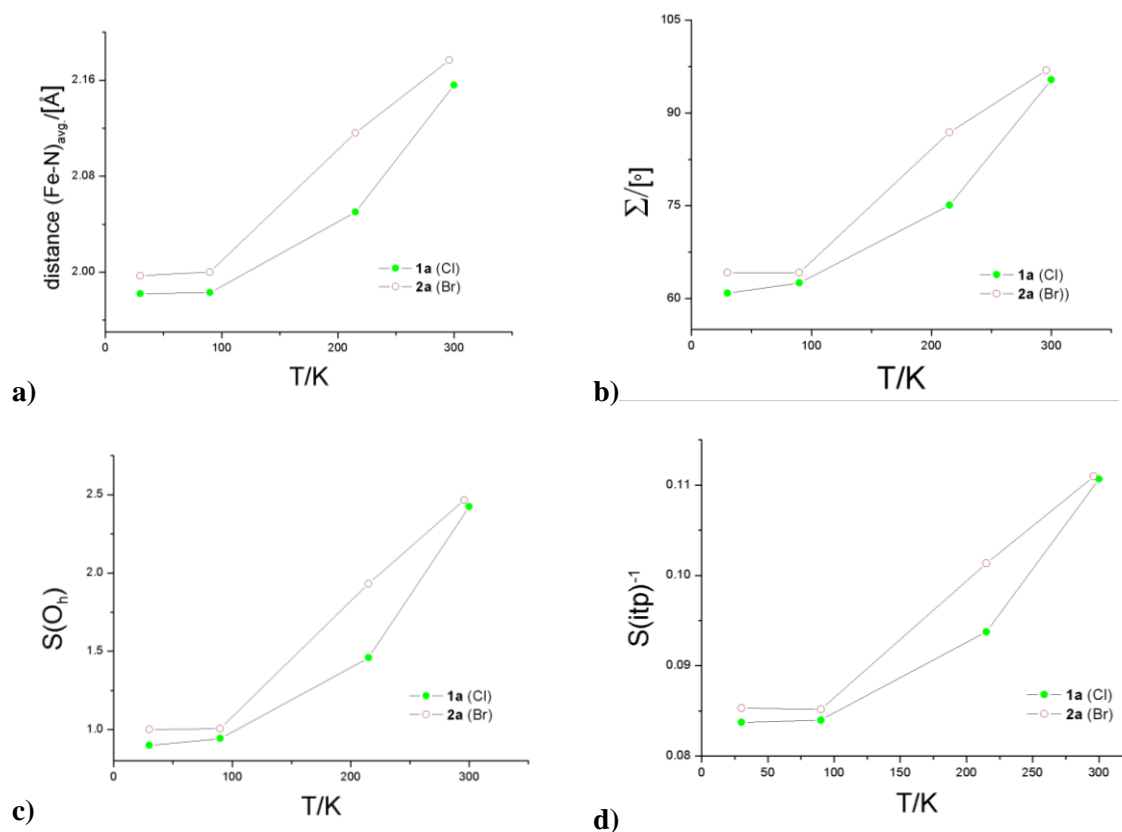
Figure 3.14: Plots of $d_{(Fe-N)avg}$ (a), Octahedral distortion factor (Σ) (b) and continuous symmetry measurements of FeN_6 core relative to ideal octahedron (c) or ideal trigonal prism (d, drawn as $S(itp)^{-1}$) vs. temperature for iron center (the two centers are crystallographically equivalents) in compounds **1a** and **2a** , as determined from single crystal X-ray diffraction data.

The Plots of (Fe-N)$_{avg}$, distortion parameters Σ and Θ, and continuous symmetry measures $S(Oh)$ and $S(itp)$ with temperature indicate gradual SCO behavior in the range 100-300 K (Figure 3.14 and AII.2). The values of these parameters at high or low temperatures are similar to the one observed for Fe2 of compound **1** in HS or LS state, respectively. This indicates the SCO from [LS-LS] to [HS-HS] in **1a** which agree with bulk magnetic studies that show two-step SCO centered at $T_{1/2}$ (1) = 264 K and $T_{1/2}$ (2) = 152 K. The values of these parameters at 215 K is in average between the HS and the LS states since it is locate in the center of the two-step SCO transition.

As observed in compound **1**, the Fe1···Fe1 intrahelical distance, intermolecular interactions and hydrogen bonds within **1a** have been affected also significantly by the SCO as seen in Table 3.9. The cell parameters show a gradual increase (Figure 3.15) which can be mainly ascribed to thermal expansion of the lattice and indicate no effect of the gradual SCO behavior on these parameters as seen previously in **1.**
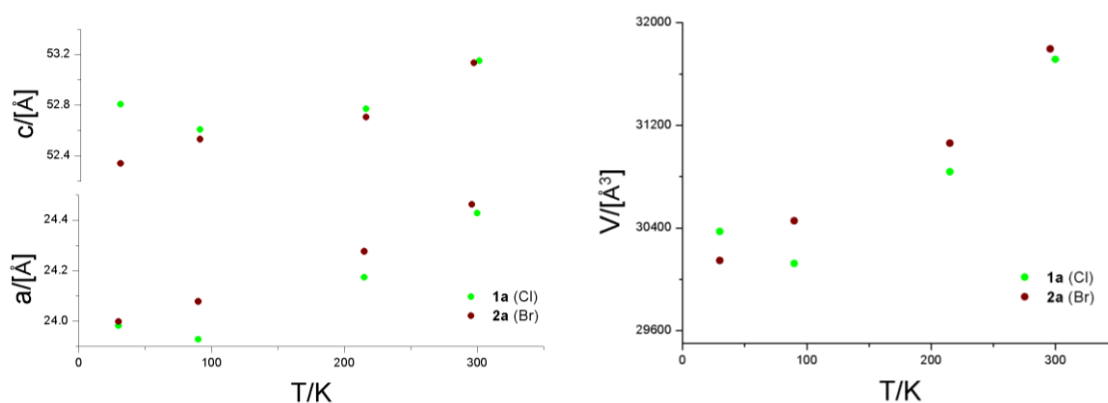
Figure 3.15: Plot of cell parameters change (Cell lengths *a* and *c* and cell volume) associated with increasing the temperature in compounds **1a** and **2a**.

Table 3.7: Crystal data for compound **1a**.

Formula	$C_{66}H_{48}Fe_2N_{18}$, $2(PF_6)$, $3(CH_4O)$, $2(Cl)$, H_2O			
FW (g mol^{-1})	1679.90			
Wavelength (Å)	0.77490			
Crystal system	tetragonal			
Space group	$I4_1$/acd			
Z	16			
T (K)	30(5)	90(2)	215(2)	300(2)
a (Å)	23.982(2)	23.9291(11)	24.1732(8)	24.4268(7)
c (Å)	52.808(6)	52.607(3)	52.773(2)	53.1521(19)
V (Å^3)	30372(6)	30123(3)	30838(2)	31714(2)
ρ_{calcd} (g cm^{-3})	1.469	1.481	1.446	1.406
μ (mm^{-1})	0.734	0.740	0.723	0.703
Independent reflections	6485	6435	6127	6768
restraints / parameters	15 / 513	27 / 513	63 / 509	23 / 501
Goodness-of-fit on F^2	1.057	1.124	1.140	1.116
Final R_1 / wR_2 [$I>2\sigma(I)$]	0.0864 /	0.1195 /	0.1539 /	0.0929 /
	0.2653	0.3200	0.3929	0.2773
Final R_1 / wR_2 [all data]	0.1015 /	0.1291 /	0.1656 /	0.1185 /
	0.2852	0.3276	0.4008	0.3038
largest diff. peak and hole	1.538 /	1.235 /	1.251 /	0.680 /
(*e* Å^3)	–1.244	–1.194	–0.916	–0.884

Table 3.8: Metal ligand Fe–N bond lengths (Å) and selected structural parameters in **1a**.

T (K)	30(5)	90(2)	215(2)	300(2)
Fe1–N2	1.947(5)	1.954(7)	2.005(13)	2.120(6)
Fe1–N5#1	1.954(5)	1.947(7)	2.012(10)	2.110(5)
Fe1–N8	1.974(5)	1.987(7)	2.046(10)	2.125(5)
Fe1–N1	1.981(5)	1.973(7)	2.019(14)	2.170(5)
Fe1–N6#1	2.015(5)	2.009(7)	2.089(9)	2.199(5)
Fe1–N7	2.019(5)	2.032(7)	2.111(9)	2.210(5)
$(Fe-N)_{avg}$	1.982	1.984	2.047	2.156
Σ (°)	60.9	62.5	75.1	95.4
Θ (°)	184.1	188.0	244.1	282.9
$S(Oh)$	0.898	0.942	1.458	2.425
$S(itp)$	11.945	11.909	10.666	9.036
V_{oct}	10.21	10.22	11.14	12.81

Symmetry operation: #1:x-0.25, y+0.25, 1.25-z

Table 3.9: Selected interatomic distances [Å] found in **1a**.

Temperature (K)	30	90	215	300
Fe1···Fe2	9.715	9.675	9.739	9.799
Fe1···Cl1	4.858	4.838	4.870	4.901
N3-H···Cl1	2.729	2.753	2.691	2.689
N4-H···Cl1	2.855	2.808	2.768	2.792
N9-H···Cl1	3.122	3.105	3.197	3.312
N9-H···Cl2	2.010	2.271	2.097	2.114
N4-H···O1S	2.417	2.405	2.608	2.657
Cl2···O1S	3.011	3.000	3.028	3.078
Cl2···O1W	2.757	2.741	2.795	2.785

3.5 Crystal Structure of $Br \subset [Fe_2(H_2L4)_3]Br(PF_6)_2 \cdot 1CH_3OH \cdot 1H_2O$ (2a)

Similar to what seen in **1a**, single-crystal to single-crystal transformation could be achieved from the methanol solvate helicate **2** to the water solvate helicate **2a** after exposing the crystals to ambient air for 5 days. The helicate is now centrosymmetric which crystallizes in the tetragonal space group $I4_1acd$ ($Z=16$). Crystallographic data and structural parameters at 90 K are shown in Tables 3.10 and 3.11. Solvents molecules are now one methanol molecules disordered over two positions by symmetry and one diffused water molecule which was determined using PLATON SQUEEZE function.[4] Now the outer Br^- is disordered over three positions. This disorder in the Br^- is more complicated than the one seen for Cl^- in **1a**. Two of these disordered positions sharing the same sphere as PF_6^- ions which itself disordered over two positions (Figure 3.16, PF_6^- is not shown). Two of the Br^- positions are close to the helicate and

participating in hydrogen bonds with N-H groups [N9-H⋯Br2 = 2.104 and N3-H⋯Br3A = 2.566 Å]. The encapsulated bromide Br1 is now in the center of the cavity [Fe1⋯Br1 = 4.847 Å] and participating in similar hydrogen bonds with the two sides of the helicate [N3-H⋯Br1 = 2.104, N4H⋯Br1 = 2.566 and N9-H⋯Br1 = 2.794Å] (Figure 3.16). As in **1a**, the two Fe(II) ions are crystallographically identical as a result of the disorder of Br⁻ ion and MeOH molecule which locate either near one side of the helicate or the other side.
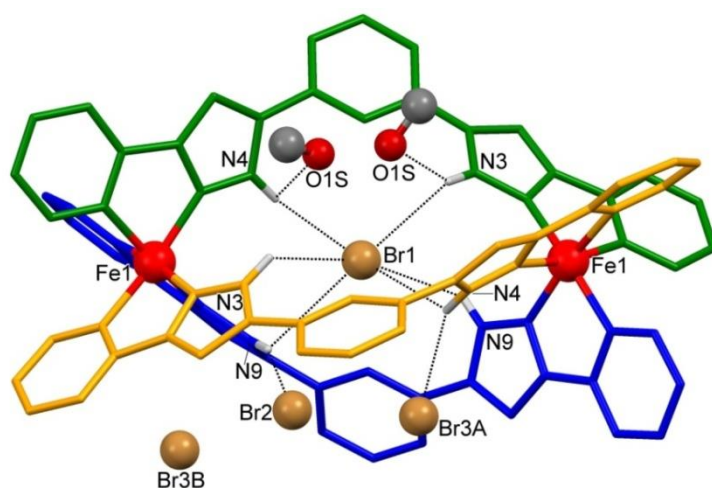
Figure 3.16: Molecular representation of $\{Br{\subset}[Fe_2(H_2L4)_3)Br]\}^{2+}$ in **2a** showing the disorder in the outer Br over three positions (Br2, Br3A and Br3) and the disorder of CH_3OH over two positions. The hydrogen bonding with N-H groups is shown. PF_6^- ions are omitted for clarity. Only the hydrogen atoms on the pyrazole nitrogen atoms are shown. Only metals and heteroatoms involved in hydrogen bonding are labeled

Variable temperatures crystal structure measurements at 30, 90, 195 and 296 K (Tables 3.10 and 3.11) indicate a similar SCO behavior as in **1a**. The thermal curves of (Fe-N)$_{avg}$, distortion parameter Σ and Θ, and the continuous symmetry measures $S(O_h)$ and $S(itp)$ are shifted to lower temperatures in comparison to compound **1a** (Figure 3.14 and AII.2) by around 30 K. This behavior is consistent with bulk magnetic properties which show similar shift in the deduced $T_{1/2}$ value. Again stronger hydrogen bonds in Cl⁻ stabilize LS state in the iron centers more than Br⁻. Again the change in the intermolecular interactions and hydrogen bonds in addition to the cell parameters with temperature is similar to the one seen in **1a** (Table 3.12 and Figure 3.15).
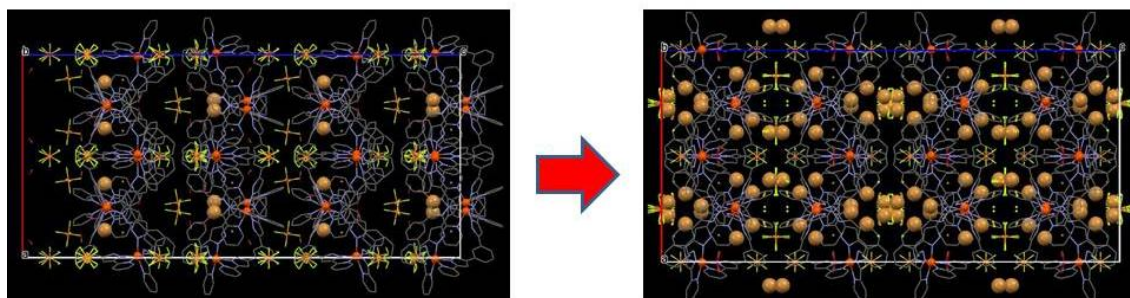
Figure 3.17: Representation of the unit cell of **2** and **2a**, emphasizing the disorder exhibited by the out-of-helicate Br$^-$ (represented in brown space filling format) that result from the MeOH exchange by H_2O. Here the disorder is more complicated than the one seen in **1a**. The Fe atoms of each helicate are represented as orange balls. The remaining atoms are represented in wireframe format

Table 3.10: Crystal data for compound **2a**.

Formula	$C_{66}H_{48}Fe_2N_{18}$, 2(F_6P), CH_4O, 2(Br), H_2O			
FW (g mol^{-1})	1704.74			
Wavelength (Å)	0.77490			
Crystal system	tetragonal			
Space group	$I4_1$/acd			
Z	16			
T (K)	30(5)	90(2)	195(2)	296(2)
a (Å)	23.999(4)	24.078(2)	24.276(3)	24.462(3)
c (Å)	52.340(8)	52.531(6)	52.706(7)	53.134(8)
V (Å^3)	30145(11)	30456(7)	31061(9)	31795(9)
ρ_{calcd} (g cm^{-3})	1.506	1.487	1.462	1.424
μ (mm^{-1})	1.974	1.955	1.916	1.868
Independent reflections	8311	8412	8258	8089
restraints / parameters	328 / 593	328 / 593	493 / 616	499 / 616
Goodness-of-fit on F^2	1.072	1.072	1.084	1.081
Final R_1 / wR_2 [$I>2\sigma(I)$]	0.0865 / 0.2547	0.0876 / 0.2641	0.1067 / 0.3254	0.0908 / 0.2445
Final R_1 / wR_2 [all data]	0.1110 / 0.2841	0.1026 / 0.2812	0.1271 / 0.3435	0.1232 / 0.2703
largest diff. peak and hole (e Å^3)	2.277 / −1.675	2.262 / −2.022	1.505 / −1.802	1.336 / −1.194

The organization of **2a** in the lattice is similar to the previous compounds consisting of sheets of $\{Br \subset [Fe_2(H_2L4)_3]\}^{3+}$ helicate connecting through $\pi-\pi$ and C-H$\cdots\pi$ interactions of the aromatic rings. This $\pi-\pi$ interactions are similar to what observed in **1** (see Figure 3.4) where now centroid to centroid distance is the same around the helicates and equal to 3.846 Å. These sheets are again in parallel with

hydrophilic layers contain solvent molecules and anions which facilitates the solvent exchange without losing crystallinity. Figure 3.17 illustrate the transformation in the unit cell of **2** as a result of solvent exchange with environment to form **2a.** Here the disorder exhibited by the out-of-helicate Br^- is complicated since it's happen over three positions where one of them is disordered again by symmetry. However, this disorder in Br^- in addition to the disorder in MeOH molecule made similar environment around both Fe centers resulting in different magnetic behavior than the original crystals (see below).

Table 3.11: Metal ligand Fe–N bond lengths (Å) and selected structural parameters in **2a**.

T (K)	30(5)	90(2)	195(2)	296(2)
Fe1–N2	1.965(5)	1.967(5)	2.077(7)	2.134(5)
Fe1–N5#1	1.978(5)	1.983(4)	2.073(6)	2.141(5)
Fe1–N1	1.986(5)	1.988(5)	2.122(8)	2.183(5)
Fe1–N8	1.989(5)	1.992(5)	2.090(7)	2.153(5)
Fe1–N6#1	2.028(5)	2.034(5)	2.154(6)	2.221(5)
Fe1–N7	2.033(5)	2.034(4)	2.176(6)	2.227(5)
$(Fe-N)_{avg}$	1.996	2.000	2.115	2.176
Σ (°)	64.18	64.19	86.88	96.92
Θ (°)	194.0	194.7	257.2	288.1
$S(Oh)$	0.999	1.006	1.932	2.467
$S(itp)$	11.721	11.741	9.871	9.013
V_{oct}	10.42	10.47	12.20	13.18

Table 3.12: Selected interatomic distances [Å] found in **2a**.

| Temperature (K)	30	90	195	296
Fe1···Fe2	9.668	9.694	9.752	9.786
Fe1···Br1	4.834	4.847	4.876	4.893
N3-H···Br1	2.750	2.747	2.692	2.723
N4-H···Br1	2.842	2.851	2.806	2.819
N9-H···Br1	3.141	3.146	3.271	3.325
N9-H···Br2	2.099	2.104	2.139	2.180
N4-H···Br3A	2.541	2.566	2.637	2.764
N3-H···O1S	2.741	2.794	3.018	3.244

3.6 Encapsulating Ability of the $[Fe_2(H_2L)_3]^{4+}$ Host

The above structural studies show that the host helicate $[Fe_2(H_2L)_3]^{4+}$ is capable of encapsulating Cl^- or Br^-, while not being able of hosting I^- in its central cavity. Indeed, all attempts to prepare a hypothetical $\{I \subset [Fe_2(H_2L)_3]\}^{3+}$ species failed, eventually even

leading to the new product Cl⊂[Fe$_2$(H$_2$L4)$_3$](I$_3$)$_3$.3(Et$_2$O) (**3**) (see the following section), resulting from the presence of Cl$^-$ traces in the system.

The so-called packing coefficient has been previously employed to evaluate the possibility of encapsulating guests within a host cavity and its efficiency.[5–7] The packing coefficient, *PC*, of a host/guest system is the ratio of the volume of the guest over that of the host cavity (*PC=V$_{guest}$/V$_{cav,}$). The ideal packing coefficient for the case of encapsulation of liquids was shown to be 0.55 ± 0.09.[5] Higher values (0.60 – 0.79) have been found with host/guest systems involving strong intermolecular interactions.[8] The volume of the cavity inside the [Fe$_2$(H$_2$L4)$_3$]$^{4+}$ host was calculated from the molecular structure of compounds **1** and **2** as 28 and 33 Å^3, respectively, using Swiss-Pdb Viewer 4.1 (Figure 3.18). The difference suggests that this host has a certain degree of flexibility and is capable to adjust its size depending on the nature of the guest. On the other hand, the volume of halide ions was calculated from their radii as 19.51, 25.52 and 36.62 Å^3, for Cl$^-$, Br$^-$ and I$^-$, respectively.[9] The calculated *PC* values for Cl$^-$ and Br$^-$ in **1** and **2** are 0.697 and 0.773, respectively. These higher than the ideal value (0.55) numbers are expected, considering the strong N–H···X$^-$ H-bonding interactions involved in these host/guest systems. In addition, it is possible that for the case of monoatomic anions (such as halides) the ideal *PC* value is larger than for liquids. For the case of I$^-$, it appears indeed that the volume of the anion seems excessive to accommodate within this host.
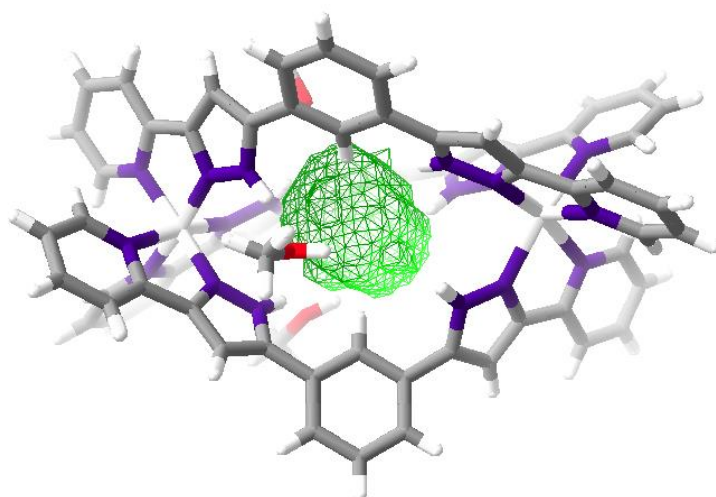
Figure 3.18: Crystal structure of **1** with the anions removed and with the volume of the central cavity highlighted as green surface using Swiss-Pdb Viewer 4.1 (Cavity Volume = 28 Å^3).

3.7 Synthesis and Crystal Structure of Cl⊂[Fe₂(H₂L4)₃](I₃)₃·3(Et₂O) (3)

Following continuous attempts to obtain an I⁻ encapsulated helicate using FeI₂ salts, only a crystals of the compound Cl⊂[Fe₂(H₂L4)₃](I₃)₃.3(Et₂O) (**3**) could be obtained, formed thanks to the presence of traces of Cl⁻ ions in the reactants or the glassware. It was possible to reproduce the synthesis directly from the reaction of FeCl₂ with H₂L4 in CH₃OH and combining the resulted mixture with a methanolic solution of NBu₄I. Slow diffusion of ether into the resulting mixture yielded red crystals after few days in good yield and reproducibility.
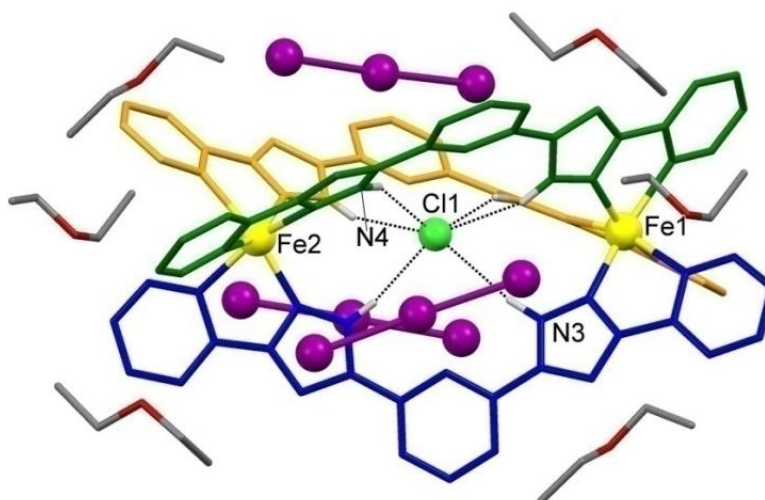
**Figure 3.19**: Molecular structure of of Cl⊂[Fe₂(H₂L4)₃](I₃)₃ **3** and the six surrounding molecules of Et₂O. Cl···H-N hydrogen bond is shown. The three ligand strands are in different colors, Et₂O in red and grey, and I in purple. Only Fe(II), and Cl⁻ are labeled. Only the hydrogen atoms on the pyrazole nitrogen atoms are shown in white.

Compound **3** crystallizes in the trigonal space group $R\bar{3}$ (Z=6). Crystallographic data and structural parameters at 90 K are shown in Tables 3.13 and 3.14. The structure contains an encapsulating helicate {Cl⊂[Fe₂(H₂L4)₃]}³⁺ similar to the one shown in compounds **1** and **1a**. The counter ions are now three triodide (I₃⁻) linear ions occupying the outer space formed between the helical strands. The Cl⁻ ion is closer to one of the iron centers, making them crystallographically different [Fe1···Cl1= 5.036 Å, Fe2···Cl1= 4.768 Å]. Cl1⁻ is involved in hydrogen bonding with the N-H groups, which are stronger in one side than the other [N3-H···Cl1 = 2.641 and N4-H···Cl1 = 2.545 Å].

At 100 K, both iron ions have HS configuration [(Fe1-N)ₐᵥg = 2.185, (Fe2-N)ₐᵥg = 2.188 Å]. This behavior is different than that observed with previous helicates. This could be a

consequence of the absence of hydrogen bonds with other counter ions or solvents out of the cavity as observed before. However, here the interaction of N-H groups with only Cl$^-$ ion stabilizes the HS, which agrees with what was observed in compounds **1** and **2** (Table 3.15). The Fe1$\cdots$Fe2 distance is 9.804 Å, which is significantly longer than that observed in compound **1** (9.731 Å at 100 K). This is expected since now the two iron ions exhibit the HS states, where as in **1**, they exhibit HS-LS states at this temperature.

The distortion parameters Σ and Θ exhibit values [$\Sigma = 106.6$ and 110.8°, $\Theta = 331.7$ and 335.7° for Fe1 and Fe2, respectively] similar to the one seen around Fe1 in compound **1** [$\Sigma = 113.56°$, $\Theta = 337.4$] since all of them exhibit the HS state. These values are close to these observed around Fe1 ($\Sigma = 113.56°$) in **1** since all of them exhibit the HS state. Continuous symmetry measures [$S(Oh)$ and $S(itp)$] show an average value of 3.50 and 6.12, respectively. These values is agree with the values observed for HS Fe(II) center in **1** at 100 K [$S(Oh) = 3.52$ and $S(itp) = 7.26$].
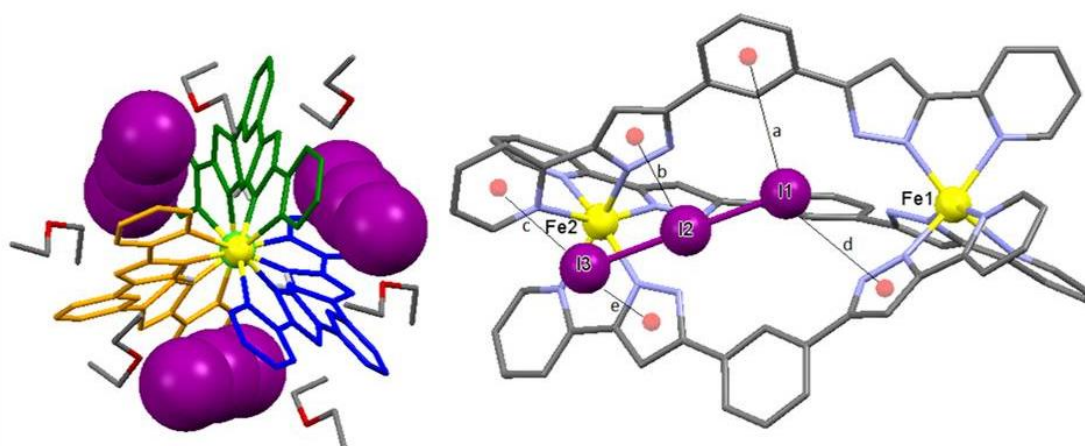
Figure 3.20: left) Representation of Cl⊂[Fe$_2$(H$_2$L4)$_3$](I$_3$)$_3$ **3** and the six surrounding Et$_2$O molecules along the C axis, emphasizing the accommodation of the I$_3^-$ (as space fill style) between the ligand strands. Right) Representation of the "lone pair-π" interactions between the I$_3^-$ groups with the aromatic rings of the ligands. Centroid to atoms distances (Å) in **3** and **4** (analogous structure); (a) 4.148/4.151, (b) 3.939/3.971,(c) 4.012/3.999, (d) 3.956/3.995, 3.978/3.954 Å.

The location of the I$_3^-$ ions between the ligand strands allows for "lone pair-π" interactions of I$_3^-$ with several aromatic rings. In fact, a total of six contacts fulfill the criteria to consider such interaction[10] as rare example where the three atoms of the anion interact with one or more aromatic rings (Figure 3.20). This interaction causes the

pyrazolylpyridine group on one side of the ligand to be almost within the plane of the central phenylene (mutual angle of 10.3°) whereas on the other side, the pyrazolylpyridine is twisted by 29.96° with respect to the central phenylene group. Figure 3.20 illustrates these lone pair-π interactions which have values between 3.939 and 4.148 Å.
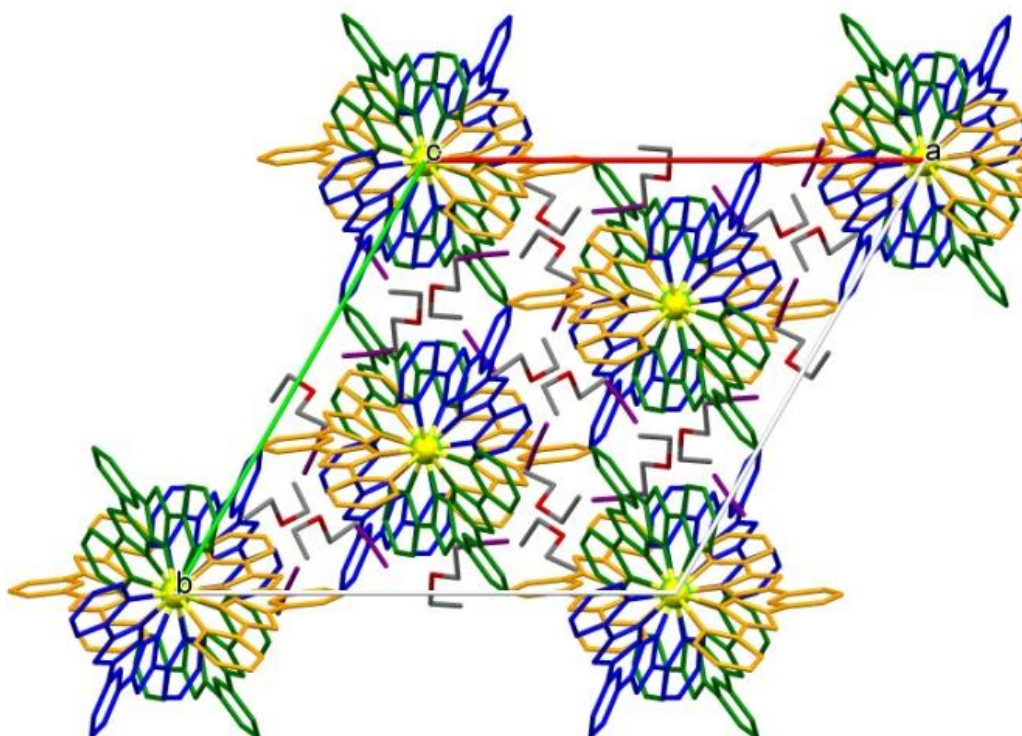
Figure 3.21: Representation of the lattice packing in Cl⊂[Fe$_2$(H$_2$L4)$_3$](I$_3$)$_3$ **3** as rods along the *c* axis separated by solvent molecules. Hydrogen atoms are not shown. The same packing feature observed in **4**.

The packing of the lattice in **3** consists of infinite rods parallel to the *z* axis and along the Fe···Fe helical axis (Figure 3.21). This feature is different from the packing observed in the previous helicates, which show layers-type packing. Now, the Et$_2$O solvents are located between these infinite rods. The rods are mutually shifted and interact together through weak π-π interactions between the aromatic rings. As seen in Figure 3.22, each central helicate is surrounded by six neighbor molecules that interact through their central phenylene groups.
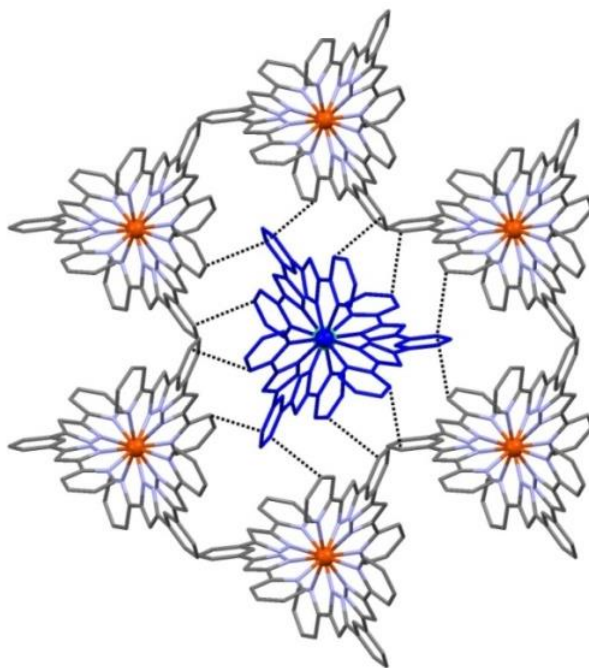
Figure 3.22: Representation of the interaction between a central helicate $\{Cl \subset [Fe_2(H_2L4)_3]\}^{3+}$ of **3** (Blue) along the C axis with six surrounded neighbors helicates showing the π-π interactions formed by the latter as shortest C⋯C contacts between the concerned rings. The same interaction observed in **4**.

Table 3.13: Crystal data for compounds **3** and **4**.

Compound	**3**	**4**
Formula	$C_{66}H_{48}Fe_2N_{18}$, $3(C_4H_{10}O)$, $3(I_3)$, Cl	$C_{66}H_{48}Fe_2N_{18}$, $3(C_4H_{10}O)$, $3(I_3)$, Br
FW (g mol^{-1})	2604.83	2649.29
Wavelength (Å)	0.71073	0.71073
Crystal system	trigonal	trigonal
Space group	$R\overline{3}$	$R\overline{3}$
Z	6	6
T (K)	100(2)	100(2)
a (Å)	19.1136(4)	19.1229(6)
c (Å)	41.1375(11)	41.0582(15)
V (Å^3)	13015.3(6)	13002.8(9)
ρ_{calcd} (g cm^{-3})	1.994	2.030
μ (mm^{-1})	3.625	4.058
Independent reflections	8322	6596
restraints / parameters	0 / 339	0 / 340
Goodness-of-fit on F^2	1.007	1.055
Final R_1 / wR_2 [$I>2\sigma(I)$]	0.0304 / 0.0766	0.0302 / 0.0784
Final R_1 / wR_2 [all data]	0.0416 / 0.0812	0.0345 / 0.0808
largest diff. peak and hole (e Å^3)	2.132 / –0.969	2.424 / –1.030

3.8 Synthesis and Crystal Structure of Br⊂[Fe$_2$(H$_2$L4)$_3$](I$_3$)$_3$·3(Et$_2$O) (4)

Compound **4** is isostructural to **3**, where now the halide ion is Br$^-$. The synthesis procedure was the same, using FeBr$_2$ as iron salt instead of FeCl$_2$. **4** crystallizes also in the trigonal space group $R\overline{3}$ (Z=6). The structure contains now an encapsulating helicate {Br⊂[Fe$_2$(H$_2$L4)$_3$]}$^{3+}$ and the charge is compensated again with three triodide (I$_3^-$) linear ions (Figure 3.23). The difference in X···Fe distances is smaller than that observed in **3** [Fe1···Br1= 4.938 Å, Fe2···Br1= 4.824 Å] while the difference in the hydrogen bonds with the pyrazole moiety in both helical sides are much greater in **4** [N4-H···Br1 = 2.726 and N3-H···Br1 = 2.967 Å] (Table 3.15). However, as in **3** both Fe(II) centers have HS state at 100 K ((Fe1-N)$_{avg}$ = 2.191, (Fe2-N)$_{avg}$ = 2.192 Å).

Table 3.14: Metal ligand Fe–N bond lengths (Å) and some structural parameters in **3** and **4**.

|	**3**	**4**
Fe1–N2	2.129(2)	2.139(3)
Fe1–N1	2.240(3)	2.243(3)
Fe2–N5	2.142(2)	2.148(3)
Fe2–N6	2.234(2)	2.235(3)
(Fe1-N)$_{avg}$	2.185	2.191
(Fe2-N)$_{avg}$	2.189	2.192
Σ (°)^a	106.6/110.78	107.56/109.04
Θ (°)^a	331.7/335.7	330.5/326.7
$S(Oh)^a$	3.383/3.610	3.322/3.303
$S(itp)^a$	6.344/5.896	6.497/6.450
V_{oct} (Å^3)	13.18/13.20	13.29/13.30

a) In Fe1/Fe2 form

The Fe1···F2 distance 9.762 Å is larger than that observed for Br-encapsulated helicate **2** since now both Fe(II) centers exhibit HS state. The distortion parameter Σ and the continuous symmetry measures [$S(Oh)$ and $S(itp)$] in both iron centers in **4** are close to that observed for HS Fe(II) in the previous helicates (Table 3.14). "lone pair- π" interactions of I$_3^-$ with several aromatic rings of the helicate and packing feature is similar to the that seen in compound **3** (Figure 3.20-Figure 3.22).

Table 3.15: Selected interatomic distances [Å] found in **3** and **4**.

Compound	**3**	**4**
Fe1···Fe2	9.804	9.762
Fe1···X1	5.036	4.938
Fe2···X1	4.768	4.824
N3-H···.X1	2.641	2.967
N4-H···X1	2.545	2.726
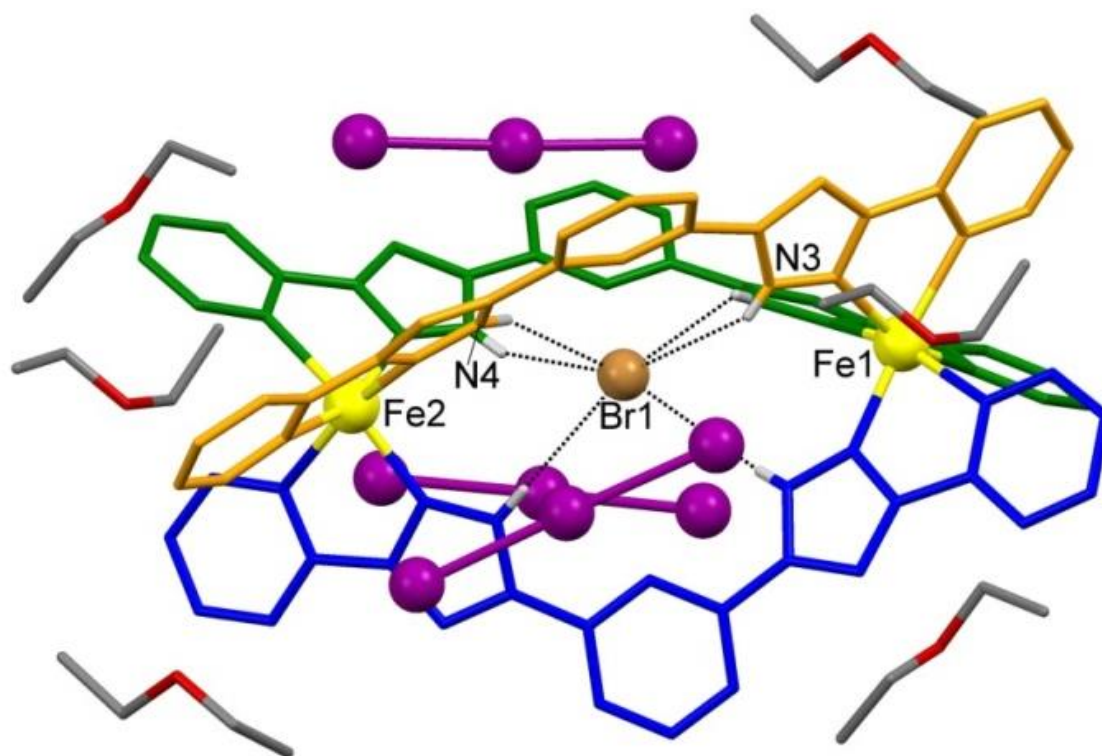
Figure 3.23: Molecular structure of Br⊂[Fe$_2$(H$_2$L4)$_3$](I$_3$)$_3$ **4** and the six surrounding molecules of Et$_2$O. The Cl...H-N hydrogen bonds are shown. The three ligand strands are in different colors, Et$_2$O in red and grey, I⁻ in purple. Only Fe(II), and Cl⁻ are labeled and only the hydrogen atoms on the pyrazole nitrogen atoms are shown in white.

## 3.9   Magnetic Properties of the X⊂Fe$_2$ Helicates

Magnetic susceptibility measurements were performed on the six helicates **1**, **2**, **1a**, **2a**, **3** and **4**, in a range from 2 K up to 350 or 380 K, using a constant magnetic field of 0.5 T. The thermal variation of $\chi_M T$ product (χ_M is the molar paramagnetic susceptibility) for these complexes is represented in Figure 3.24.

For compound **1**, the variation of $\chi_M T$ versus temperature reveals a gradual and complete SCO behavior from [HS-LS] at low temperatures to [HS-HS] at higher temperature with $T_{1/2}$ around 300 K. Below 200 K down to 25 K the value of $\chi_M T$ is constant (3.85 cm^{3}mol^{-1}K) which indicates one HS iron center (g = 2.27), consistent with crystal structure measurements below 230 K. Below 25 K, a sharp decline was observed as consequence of the zero field splitting (ZFS) of the remaining HS metal centers. The $\chi_M T$ value at 380 k is 7.15 cm^{3}mol^{-1}K which is in the range of values

expected for two non-interacting Fe(II) centers with $^5T_2$ ground state ($S = 2$, $g = 2.18$), also in agreement with the crystal structure at 340 K.

These magnetic data and the crystal structure measurements show that although both Fe(II) centers exhibit the same coordination environment they exhibit different magnetic properties. The supramolecular interactions of the helicate, especially involving the N-H groups with the halide or the methanol molecules in one side or the other of the helicate cause this different magnetic response. N-H groups close to Fe1 center interact mainly with Cl1 and Cl2 where N-H groups in the opposite side of the helicate interact mainly with MeOH solvent molecules. As a result of these interactions, the halide ions stabilize HS state in Fe1 and the MeOH molecules stabilize LS state in Fe2. The effect of the interactions with solvents or anions on the crystal field and hence the magnetic properties of the metal ion is well known.[11,12]
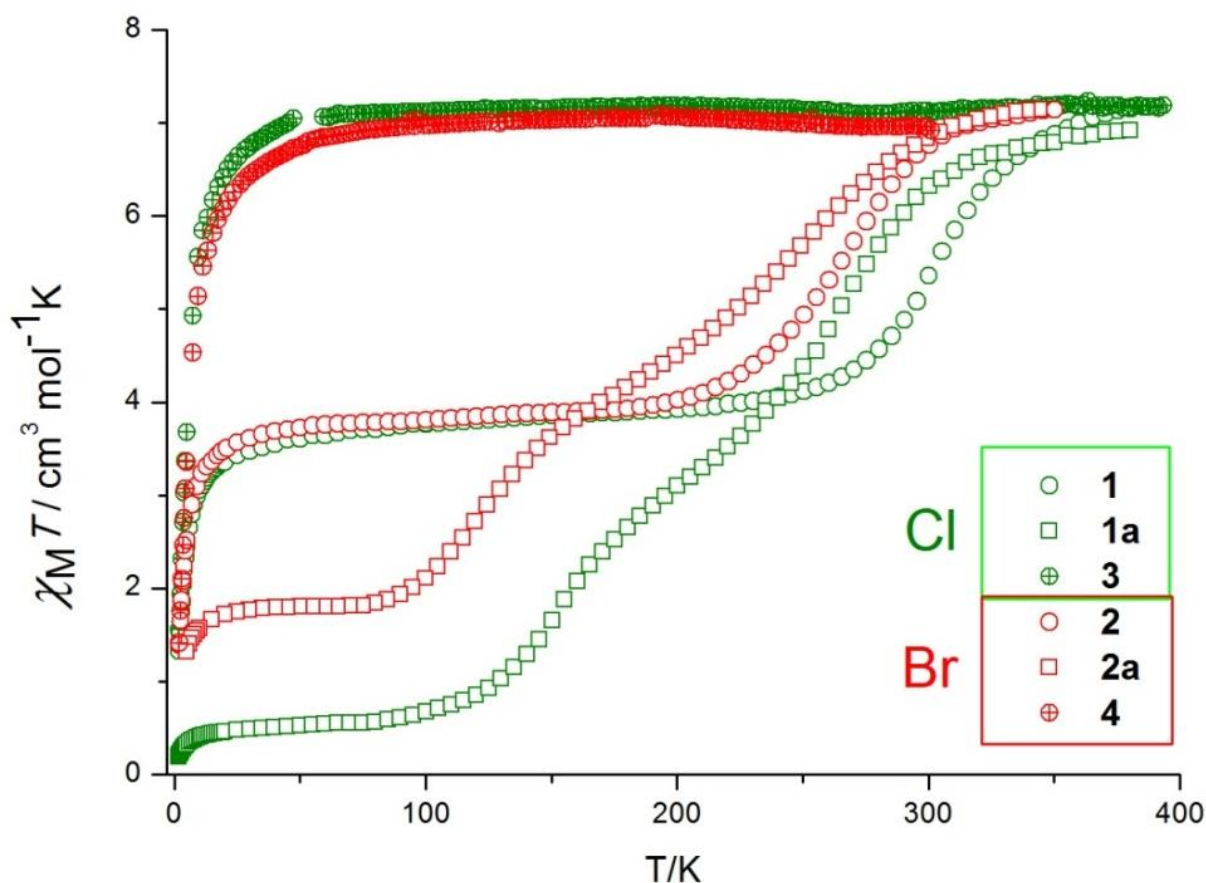

Figure 3.24: Variable temperatures magnetic measurements for the helicates **1**, **2**, **1a**, **2a**, **3** and **4** measured in 0.5T dc magnetic field.

The variation of $\chi_M T$ versus temperature in compound **2** shows also a gradual and complete SCO from [HS-LS] to [HS-HS] as seen in compound **1**. At 350 K, $\chi_M T$ value

is 7.14 $cm^3mol^{-1}K$ which indicates two HS Fe(II) centers and agrees very well with the crystal structure at 340 K. The $\chi_M T$ value starts to decrease gradually from 320 K to reach a plateau, between 190 and 40 K, with a $\chi_M T$ value of around 3.8 $cm^3mol^{-1}K$, indicating only one HS Fe(II) center. This [HS-LS] state was also seen in the crystal structure below 200 K. As in **1**, the decline below 40 K is due to ZFS for the HS Fe(II) center.

Changing the two halide ions from chloride to bromide in compound **2** produces a down shift in the $T_{1/2}$ (= 270 K) of the SCO by 30 K, comparing with the Cl$^-$ analogous. Both compounds show a similar structure where the main difference is the nature of the halide ion, yielding different X$\cdots$H-N hydrogen bond strengths and as result, affecting differently the crystal field around the iron centers. The Cl$^-$ ion stabilizes the LS state in Fe2 more than the Br$^-$ ion.
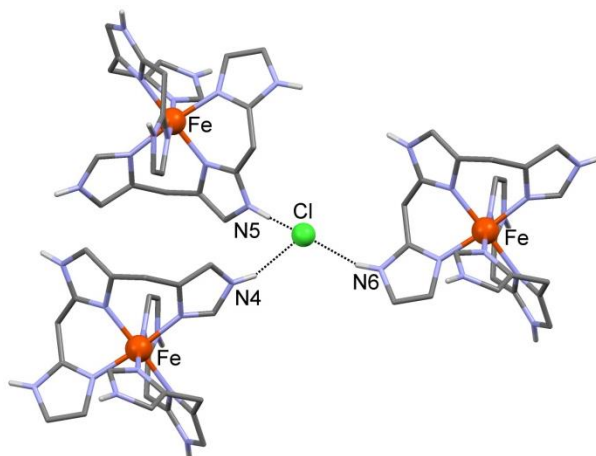

Figure 3.25: View of part of hydrogen bond network of the complex [Fe(trim)$_2$]Cl$_2$.[11] The interaction of N-H groups and Cl$^-$ is illustrated. Only the hydrogen atoms on the pyrazole nitrogen atoms are shown. Only metals and heteroatoms involved in hydrogen bonding are labeled

This behavior is in contradiction with previous observations made for [Fe(trim)$_2$]X$_2$[11] (Figure 3.25). The trend observed for T$_{1/2}$ was I$^-$(380 K) > Br$^-$(340 K) > Cl$^-$(180 K) > F$^-$ (20 K). The behavior was interpreted as an inductive effect of the halide ions, transmitted to the nitrogen donors through hydrogen bonds. An increase in inductive effect of the anion corresponds to a decrease in the SCO temperature ($T_{1/2}$). The authors compare the experimental data with those derived from DFT calculations. Interestingly, the trend observed experimentally (taking into account individual molecules) disagrees

with the spin state splitting E_s calculated for isolated molecules which show an increase in $T_{1/2}$ with the following trend $F^->Cl^->Br^->I^-$. E_s here is the difference between the energy of the HS and LS state. However, the calculation using periodic boundary conditions that include the complete unit cell show the same trend as the one observed experimentally. These reported systems have two main different features compared to the systems here described. First, the N-H pyrazole groups are in β position from the coordinated nitrogen, while in the current work the N-H groups are in α position. Second, the halide ions are making a network and interacting with three independent cation molecules. These differences could be the reason of the discrepancy between both systems.

On the other hand, there are other systems that contain N-H groups near Fe(II) SCO centers participating in hydrogen bonds with halides that show a similar trend in $T_{1/2}$ as in the current work. Coordination polymers [Fe(hyetrz)$_3$]X$_2$(hyetrz = 4-(2'-hydroxyl-ethyl)-1,2,4-triazole) and Fe(NH$_2$trz)$_3$X$_2$ (NH$_2$trz = 4-amino-1,2,4-trizole) showed an increase in $T_{1/2}$ in the following order (Cl$^->$Br$^->$I$^-$).[1,13,14] Although the crystal structure of these compounds is not determined, it is known that they exhibit hydrogen bonds between the bridging ligand and the anions.
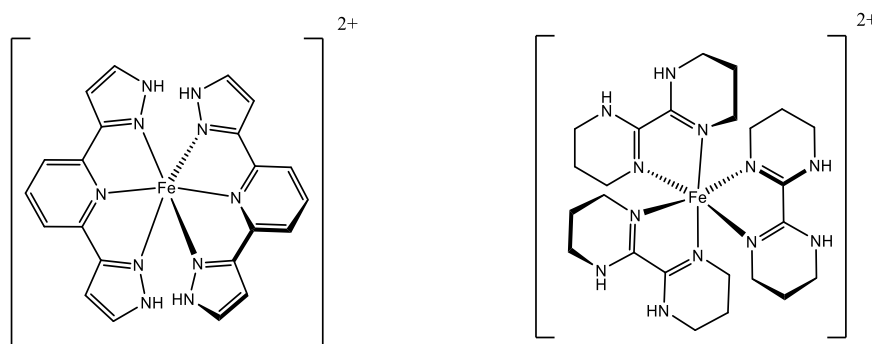
Figure 3.26: [Fe(3-bpp)$_2$]$^{2+}$ (left) and [Fe(H$_2$bip)$_3$]$^{2+}$ (right) cations used to study the effect of hydrogen bonding on $T_{1/2}$[1,15–18]. Both systems contain N-H groups capable to interact with anions via hydrogen bonding. SCO behavior in these systems shows an increase in $T_{1/2}$ with stronger associated anions.

Moreover, Halcrow et al. studied the [Fe(3-bpp)$_2$]X$_2$ (3-bpp = 2,6-di{pyrazol-3-yl}pyridine) system in solution in the presence of hydrogen bonding anions (Figure 3.26).[15] They demonstrated that strongly associated anions favor the low-spin state of the complex and increase $T_{1/2}$. For example the trend of $T_{1/2}$ follows this order, Br$^->$I$^-$

$>BF_4^->BPh_4^-$, which correlates perfectly with the hydrogen bonding ability of those anions. Moreover, Ni et al. demonstrated that the presence of Br^- anions stabilizes the low-spin states of $[Fe(H_2bip)_3]^{2+}$ and $[Fe(L)(H_2bip)_2]^{2+}$ (Figure 3.26) in the solid state and in solution[1,16–18] more than less associated anions (*eg.* BPh_4^-). These systems contain also N-H groups, in α or β with respect to the coordinated atoms. As a conclusion one can say that the trend of $T_{1/2}$ shown in these systems and in the current work show that the stronger hydrogen bonding associated with anions the more stabilized is the low spin. The reason of this behavior has not yet been fully explained.

The solvent exchange that occurred via SCSC from **1** to **1a** produces a dramatic change in the magnetic behavior of Fe(II) centers. The $\chi_M T$ value at 380 K (6.92 $cm^3mol^{-1}K$) lies in the range characteristic of [HS-HS] state of two Fe(II) centers ($g = 2.15$). Upon cooling, a gradual decrease in $\chi_M T$ is observed going through an inflection point at $T = 215$ K with $\chi_M T = 3.4$ $cm^3mol^{-1}K$. This first SCO step ([HS-HS] to [HS-LS]) is centered at $T_{1/2}$ (1) = 264 K. The $\chi_M T$ value at the inflection point corresponds to a 50% of spin conversion. This could reflect a different state of both iron centers in each molecule (*i.e.* HS-LS state) or a 1:1 mixture of [LS-LS] and [HS-HS] species. On lowering the temperature below 215 K, another gradual decrease in $\chi_M T$ is observed centered at $T_{1/2}$ (2) = 152 K to show almost a complete transition to the [LS-LS] state below 90 K with less than 6% of HS residual centers.

This SCO behavior is consistent with the crystal structure measurements; although no [HS-LS] state was distinguished at 215 K, the difference in the two iron centers is a result of the disordered Cl^- in two positions which means that the Cl^- is in one place at one time. Therefore, the two iron ions are slightly different and the crystal structure affords an average of both configurations. Moreover, the two-step SCO observed with the magnetic studies is gradual and the $T_{1/2}$ values are very close to each other, which could explain the fail to distinguish the [HS-LS] crystallographically. This hypothesis is supported by LIESST effect studies which show a meta-stable state at low temperatures corresponding to 50 % of spin conversion (*i.e.* LS-HS) (section 3.11), which could mean that both centers have indeed different responses to light irradiation due to the slight differences in the SCO behavior (*i.e.* different $T_{1/2}$ for both centers). Previous studies showed the relation between $T_{1/2}$ of thermal SCO behavior and the conversion to meta-stable HS via light irradiation.[19,20]

The effect of solvate molecules on the magnetic properties of dinuclear helicates $[Fe_2(L)_3](ClO_4)_4$ (L=bis-bidentate imidazolimine ligand) was observed by Kruger et al.[21,22] Water solvated helicates show SCO from the [HS-HS] state at high temperature to the [HS-LS] state at low temperature. Two distinct iron centers with different spin configurations were distinguished crystallographically at 150 K. In contrast, the acetonitrile solvate helicate exhibits a complete SCO transition from [HS-HS] to [LS-LS] via one-step gradual transition.

Compound **2a**, exhibits a similar behavior to **1a** with a two-step characteristic SCO. The $\chi_M T$ value at 340 K (7.13 cm^{3}mol^{-1}K) corresponds to [HS-HS] states for the Fe(II) ions. Lowering the temperature causes a gradual decrease to an inflection point at 190 K where $\chi_M T$ equals 4.2 cm^{3}mol^{-1}K. Then another gradual decrease in $\chi_M T$ occurs down to a value of 1.8 cm^{3}mol^{-1}K at 70 K, which remains constant down to 20 K. This $\chi_M T$ value corresponds to about 20 % residual HS centers which is higher than that seen in **1a**. This could be a result of incomplete solvent exchange since lower value was observed in another batch done before doing LIESST effect experiment ($\chi_M T = 1.0$ cm^{3}mol^{-1}K at low temperatures, see section 3.11). A slight decrease in $\chi_M T$ below 20 K was observed caused by ZFS of the residual HS centers. The shape of the $\chi_M T$ vs T curve in **2a** indicates also a two-step SCO centered at $T_{1/2}$ (1) = 250 K and $T_{1/2}$ (2) = 121 K. Compared with **1a**, both $T_{1/2}$ values in **2a** are shifted to lower temperatures. Again here the difference in halide ions shows the same trend in $T_{1/2}$ values as seen before, Cl$^-$ encapsulated helicates exhibit SCO at higher temperatures than these with encapsulated Br$^-$.

In contrast to helicates **1**, **1a**, **2** and **2a**, compounds **3** and **4** do not experience any SCO behavior. The $\chi_M T$ value above 50 K is 7.20 and 7.04 cm^{3}mol^{-1}K, for **3** and **4**, respectively. These values agree with two Fe(II) centers with HS configuration, which is consistent with the crystal structures at 100 K. Below 50 K, a rapid decrease in $\chi_M T$ as a result of the ZFS effects of HS Fe(II) centers is observed. Thus, although the encapsulated helical structure in **3** and **4** is similar to the helicate in **1** and **2**, the magnetic behavior is significantly different. The difference is caused by the nature of counter-anions and solvents molecules, which exhibit different interactions with the helicate. In **3** and **4**, I$_3^-$ ions exhibit lone pair-π interactions with the ligand strands, while ether molecules do not interact significantly with the helicates. The only hydrogen

bonds now are formed within the helical cavity, between the N-H groups and the encapsulated Cl^- or Br^- ions. The absence of further out-of-cavity interactions stabilizes the HS state. On the other hand, the existence of more hydrogen bonding interaction with out-of-cavity Cl^- or Br^- and methanol molecules in **1** and **2**, stabilize LS states.

## 3.10 Calorimetry (DSC) Studies of the $X{\subset}Fe_2$ Helicates

The thermal spin transition seen in **1**, **2**, **1a** and **2a** were studied in more detail using the Differential Scanning Calorimetry (DSC).

For compound **1**, the temperature dependence of the molar heat capacity at constant pressure (C_p) is shown in Figure 3.27 (left). A broad anomaly around 305 K was observed due to the SCO spin transition. The broadness and the temperature of the peak agree well with the gradual transition ($T_{1/2}$ around 300 K) found in magnetic and structural studies. The dashed line in the C_p vs. T curve represents an estimation of the normal heat capacity with the high and low temperature data. Subtracting the experimental heat capacity from the normal curve yields the excess heat capacity ΔC_p associated with the spin transition (Figure 3.27). Integrating the excess heat capacity beyond the normal heat capacity with respect to T yielded the enthalpy variation,
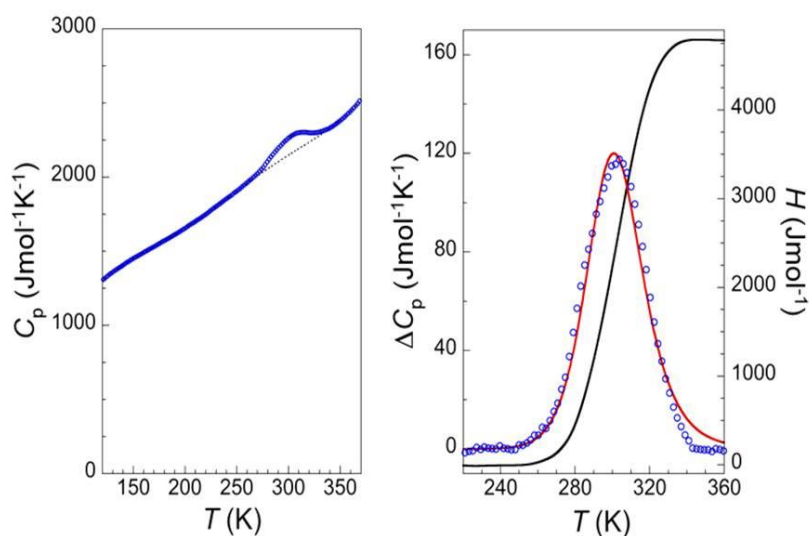
Figure 3.27: Left) Molar heat capacity of **1**, showing broad endothermic peak arising from the spin transition. Dotted curve indicates the normal heat capacity. Right) excess heat capacity (ΔC_p) beyond the normal heat capacity as a result of the spin crossover in **1** (open cycles), red solid line: fitting to Sorai's domain model with $n = 15.8$ (see text for details), black solid line: excess enthalpy involved in SCO behavior as derived from the integration of the ΔC_p vs. T.

ΔH, associated with the spin transition (4.79 KJ/mol). On the other hand, ΔS can be obtained from integrating ΔC_p with respect to lnT which yields 15.95 J/molK. These values are reasonable for a gradual SCO at high temperatures.[23–25] ΔS is only slightly higher than what would be expected from the pure electronic component of the SCO of half Fe(II) ions of the molecule ($RLn5$ = 13.38 J/molK).
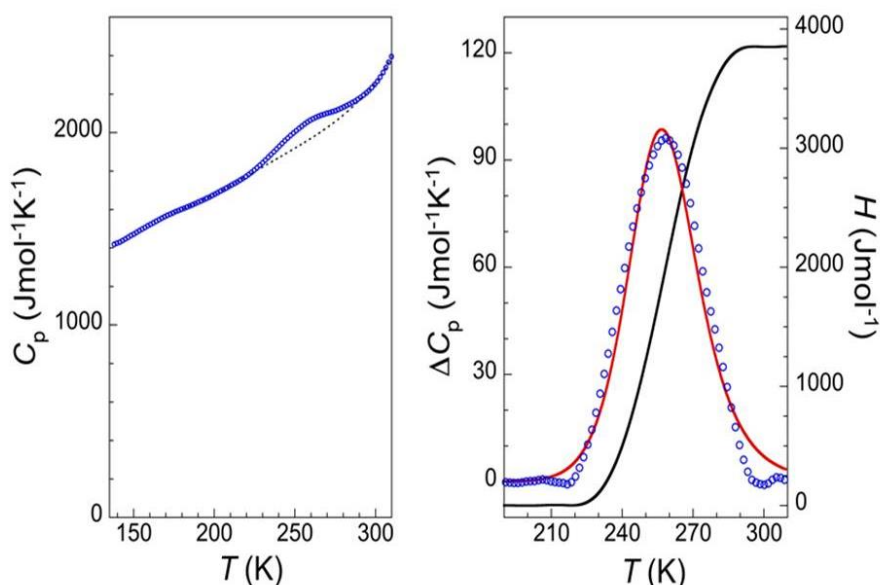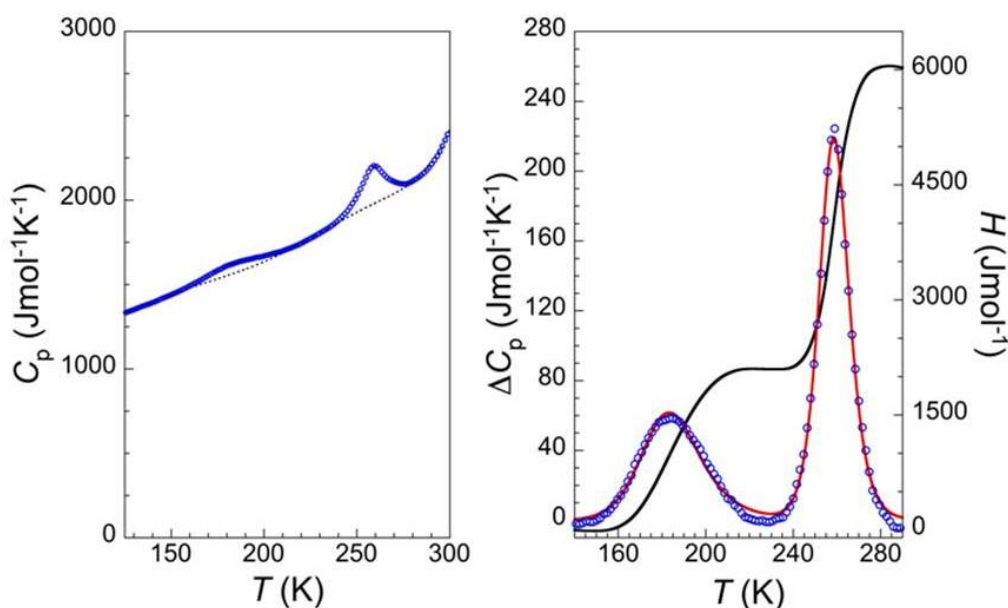

Figure 3.28: Left) Molar heat capacity of **2**, showing broad endothermic peak arising from the spin transition. Dotted curve indicates the normal heat capacity. Right) excess heat capacity beyond the normal heat capacity as a result of the spin crossover in **2** (open cycles), red solid line: fitting to Sorai's domain model with n = 14.6 (see text for details), black solid line: excess enthalpy involved in SCO behavior as derived from the integration of the ΔC_p vs. T.

With accurate calorimetric data in hand, Sorai's domain model[23] can be used to determine the domain size n (number of complexes with spin state conversion in each domain) associated with the SCO process. As the number n decreases, the heat capacity peak of the SCO process becomes broader and the cooperativity of the transition decreases.[26] Equation 1 can be used to determine the n value by fitting the thermal dependence of ΔCp.[27]

$$\Delta Cp = \frac{n(\Delta H)^2}{RT^2} \frac{\exp[\frac{n\Delta H}{R}(\frac{1}{T}-\frac{1}{T_\frac{1}{2}})]}{(1+\exp[\frac{n\Delta H}{R}(\frac{1}{T}-\frac{1}{T_\frac{1}{2}})])^2} \tag{1}$$

Fitting the data of **1** to this model (red line, Figure 3.27) gives an intermediate number of interacting centers per domain of *n*= 15.8. This value indicates week cooperativity which agrees with the gradual nature of the SCO process. This intermediate value of n and the low value of *ΔS* can be ascribed to the absence of any first order lattice modifications associated with the SCO. This agrees well with the observed cell parameters variations *vs.* temperature curves (Figure 3.9) which showed no important changes associated with the SCO behavior with the only modifications occurring at the molecular level.

Figure 3.29: Left) Molar heat capacity of **1a**, showing two broad endothermic peaks arising from the spin transition. Dotted curve indicates the normal heat capacity. Right) excess heat capacity (ΔC_p) beyond the normal heat capacity as a result of the spin crossover in **1a** (open cycles), red solid line: fitting to Sorai's domain model with *n1* = 7.0 and *n2* = 15.8 (see text for details), black solid line: excess enthalpy involved in SCO behavior as derived from the integration of the ΔC_p *vs. T*.

Similar behavior was observed for the Br⁻ analogue (**2**). A broad anomaly around 260 K was observed in the C_p *vs T* curve (Figure 3.28) consistent with the magnetic and structure measurements. The *ΔH* and *ΔS* obtained from the excess heat capacity ΔC_p are 3.85 KJ/mol and 15.01 J/molK, respectively. Moreover, fitting the data to Sorai's domain model gives here an intermediate number of interacting centers per domain n of 14.6. These values are similar to that observed in compound **1** and indicate similar thermal properties for both X-encapsulated helicates.

For compound **1a**, in the heating mode two anomalies are observed in the C_p *vs T* curve (Figure 3.29) corresponding to a two-step SCO centered at 185.0 and 258.9 K. This observation agrees with the magnetic studies, which also indicate a two-step SCO ($T_{1/2}$ (1) = 152 and $T_{1/2}$ (2) = 264 K). The differences in temperatures can be ascribed to the different heating rate used in both techniques and the very gradual nature of the SCO behavior over a broad temperature range.

Above 290 K, the heat flow continues to increase up to 390 K, likely concomitant with some solvent loss. The excess heat capacity ΔC_p *vs.* temperature is shown in Figure 3.29. The *ΔH* and *ΔS* associated with both transitions are, 2.1 KJ/mol and 11.4 J/molK, and 3.9 KJ/mol and 15.11 J/molK, respectively. *ΔS* for the low temperature transition is less than what would be expected from a pure electronic SCO process (*RLn5* = 13.38 J/molK). The large broadness in the curve may be at the root of this decreased value.

However, *ΔS* for the high temperature transition is only slightly higher than what would be expected from a pure electronic component of the SCO of half of Fe(II) ions (*RLn5* = 13.38 J/molK). The fit to Sorai's domain model gives *n1* = 7.0 and *n2* = 15.5. Again this intermediate values agree with the gradual SCO behavior observed in the magnetic studies, indicating the absence of any important lattice modifications associated with the gradual SCO in agreement with the change in cell parameters with temperature (Figure 3.15).

The similarity in *ΔH, ΔS* and *n* values in the three compounds (**1**, **2** and **1a**) indicate similar cooperativity in the three helicates. In contrast, no clear anomaly associated with the SCO was detected in DSC measurements of compound **2a**. Probably this is because of the too broad gradual SCO, which cover a wide temperature range (75-300K) seen in this system.

3.11 LIESST Effect in the X⊂Fe$_2$ Helicates

To test the possibility of recovering the HS state of the Fe(II) at low temperatures in a metastable form, LIESST effect experiments were performed in complexes **1**, **2**, **1a** and **2a**. The measurements consist of cooling the sample to 10 K in the absence of light, followed by irradiating the sample with green-light using Xe lamp and filters (500-650 nm) for a certain time (depending on the sample). Then reheating the sample in the absence of light to study the thermal relaxation of any meta-stable state.
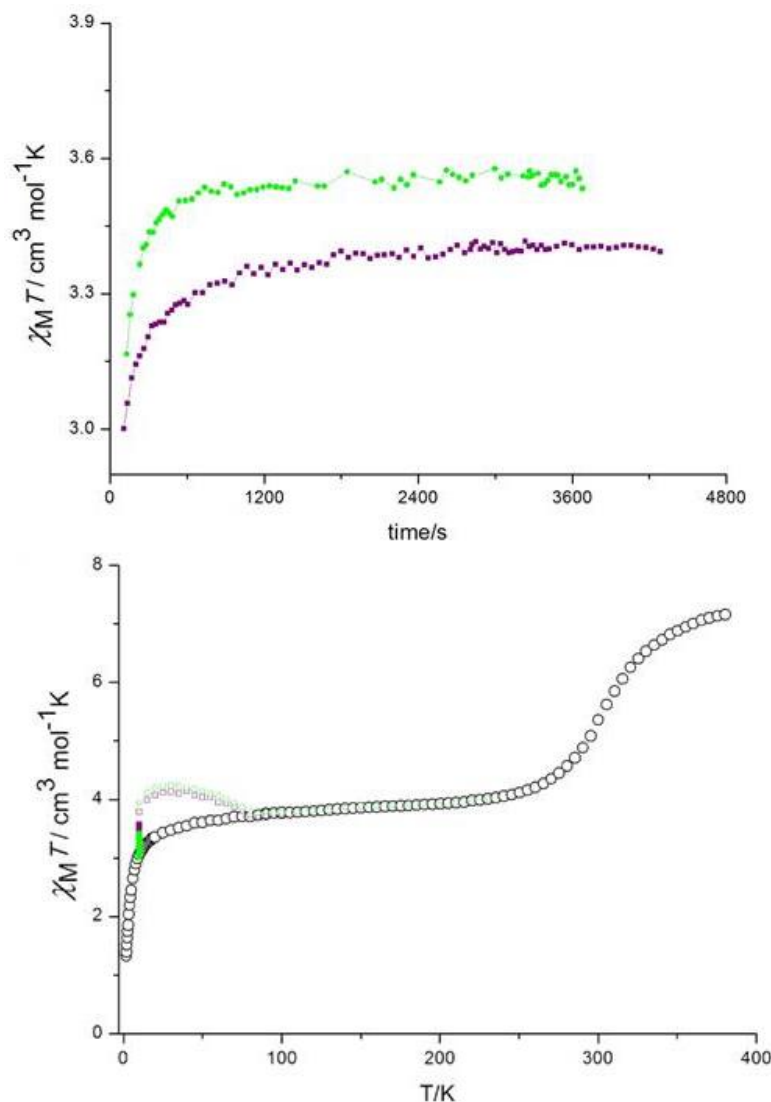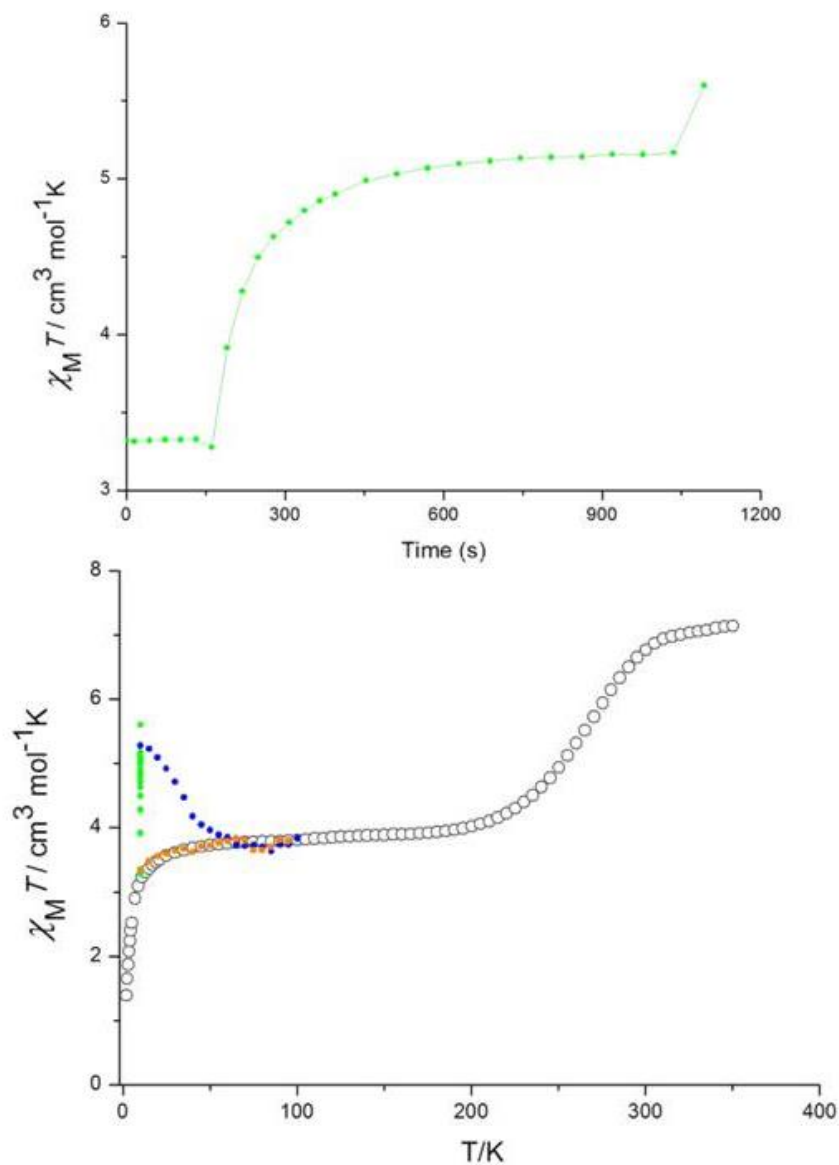
Figure 3.30: Top) Time dependence of photo-induced $\chi_m T$ value ($\lambda = 500\text{-}650$ nm) of compound **1**. Bottom) $\chi_m T$ *vs* T plot of LIESST effect experiment. Green circles represent measurements on thin pellet with mass of 1.2 mg, purple squares represent measurements on few platy crystals with mass of 0.2 mg. Open green circles, and purple squares represent the thermal dependence after switching off the light. Open gray circles represent the bulk magnetic measurements.

For compound **1**, two series of experiments were accomplished on i): a thin pellet with mass 1.2 mg (purple in Figure 3.30) and ii) a few flat crystals of 0.2 mg of mass (green in Figure 3.30). At 10 K, one Fe(II) center in the dinuclear helicateis already in the HS state. Through irradiation of light, the $\chi_m T$ value in experiment (i) increases rapidly and reaches a saturated photo-induced $\chi_m T$ value of 3.40 cm^{3}mol^{-1}K. A similar behavior was observed during experiment (ii), with only a slightly higher saturated photo-induced

$\chi_m T$ value of 3.55 cm^{3}mol^{-1}K. Taking into account that the ZFS has already an effect at the low temperature of the irradiation, this increase in $\chi_m T$ corresponds to less than 20% photo-induced conversion from [HS-LS] to [HS-HS] state.

Figure 3.31: Top) time dependence of photo-induced $\chi_m T$ value ($\lambda = 500\text{-}650$ nm) of compound **2**. Bottom) $\chi_m T$ *vs* T plot of LIESST effect experiment. Green circles represent measurements through irradiation of light. Blue circles represent the thermal dependence after switching off the light. Orange circles represent the behavior after complete relaxation. Open gray circles represent the bulk magnetic measurements before irradiation.

Since both experiments gave similar results, one can expect that the limited efficiency of photo-induced conversion is not mainly due absorption effects. The low efficiency

could be because of the competition between light induced conversion with fast HS to LS relaxation and potentially light-induced HS to LS transformation.
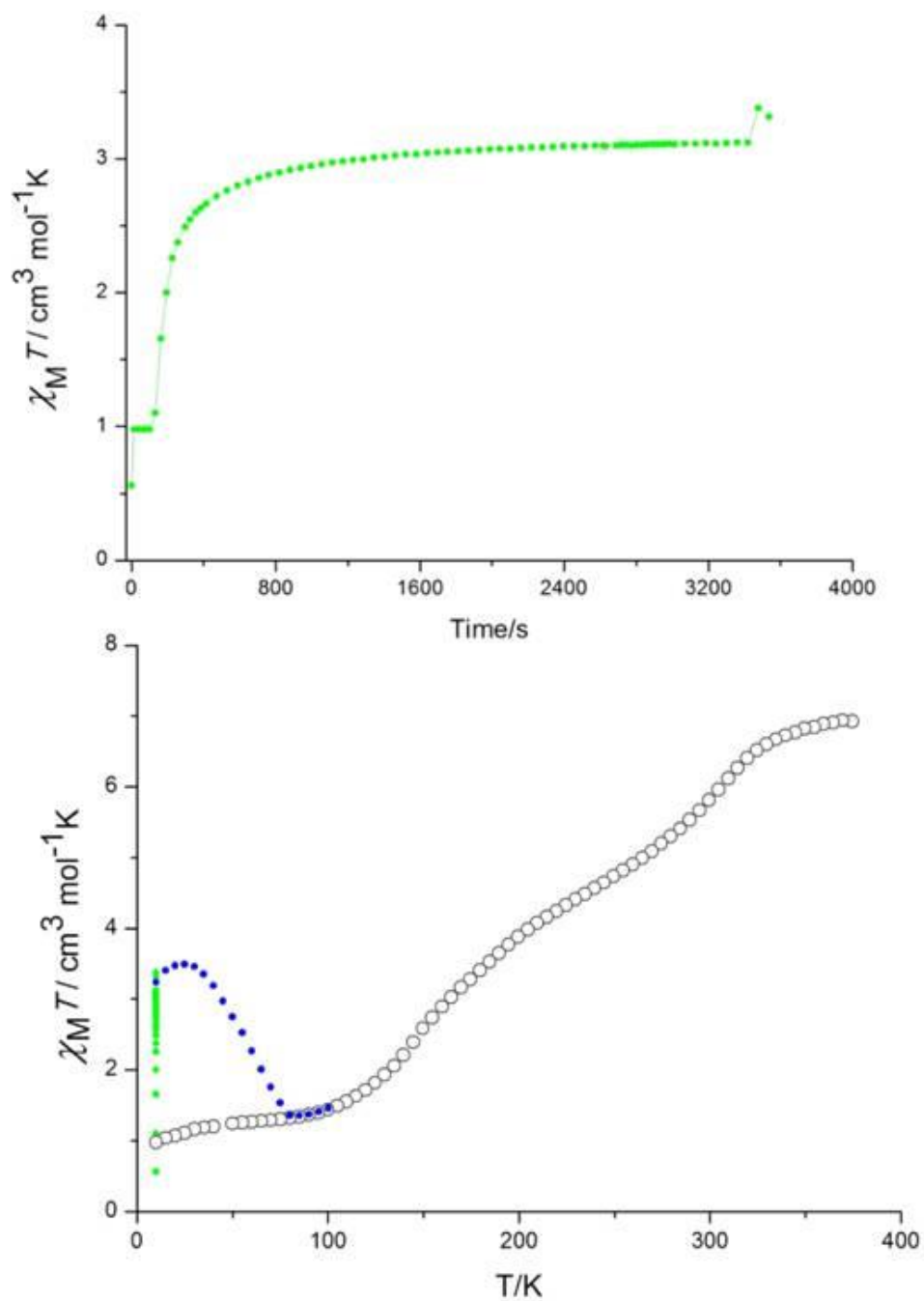
Figure 3.32: Top) Time dependence of photo-induced $\chi_m T$ value ($\lambda = 500\text{-}650$ nm) of compound **1a**. Bottom) $\chi_m T$ vs T plot of LIESST effect experiment. Green circles represent measurements through irradiation of light. Blue circles represent the thermal dependence after switching off the light. Orange circles represent $\chi_m T$ values in cooling mode after complete relaxation. Open gray circles represent the bulk magnetic measurements before irradiation.

After the light was switched off, the thermal dependence of the $\chi_m T$ value was measured. The $\chi_m T$ value increased gradually with heating reaching a maximum value of 4.2 cm^{3}mol^{-1}K at 27 K. The increase is due to the magnetic anisotropy of the HS Fe(II) centers. Above 27 K, a decrease in $\chi_m T$ was observed due to the thermal relaxation of the photo-excited state. The value of T_{LIESST} is around 73 K and the complete relaxation of the meta-stable state is observed at 82 K. The behavior above 82 K is identical to the one before irradiation.

For compound **2**, a thin sample (0.1 mg) was used for the LIESST experiment. As observed in the previous magnetic studies, the compound already exhibits the [HS-LS] state at very low temperatures. The time dependence of χT at 10 K under irradiation is shown in Figure 3.31. The $\chi_m T$ value increases quickly initially from 3.32 cm^{3}mol^{-1}K to reach photo-induced saturation with a χT value of 5.7 cm^{3}mol^{-1}K after irradiation for 18 min. Taking into account the ZFS of the original HS Fe(II) centers, this increase in $\chi_m T$ could correspond to an almost complete conversion to the [HS-HS] state. Only the competition with fast relaxation, already significant at 10 K, could impede the full excitation.

After the light was switched off, the thermal relaxation was studied as illustrated with $\chi_m T$ vs. T curve in Figure 3.31. The thermal relaxation to the LS was very fast as indicated by the rapid decrease in $\chi_m T$. The T_{LIESST} value is around 35 K, and the complete relaxation of the meta-stable state was observed at 60 K. The measurements above 60 K and through cooling after complete relaxation show identical behavior to the one before irradiation.

The measurements of **1a** at 10 K before irradiation indicate the HS state of a few residue centers ($\chi_m T = 0.98$ cm^{3}mol^{-1}K). The irradiation of **1a** with green light at 10 K causes a significant and rapid increase in the magnetization as shown in the $\chi_m T$ *vs.* time plot (Figure 3.32). A saturation of the value of χT to 3.20 cm^{3}mol^{-1}K was reached after 1 hour. This value corresponds to about half of the Fe(II) centers in the meta-stable HS state. As observed in the magnetic studies, a two-step SCO was observed [LS-LS]→[HS-LS]→[HS-HS] with $T_{1/2}$ (1) = 152 and $T_{1/2}$ (2) = 264 K. The photo induced conversion could correspond to the Fe(II) center with lower $T_{1/2}$, reaching the [HS-LS] state ($T_{1/2}$ = 152 K). In **1,** which is the MeOH solvate crystals of **1a**, less efficient LIESST effect was observed from [HS-LS] to [HS-HS] state. In **1** only one Fe(II)

exhibit SCO behavior while the other Fe(II) remain at HS over all temperatures. Previous studies showed that the higher temperature the SCO takes place, the less accessible the meta-stable HS state.[19,20]
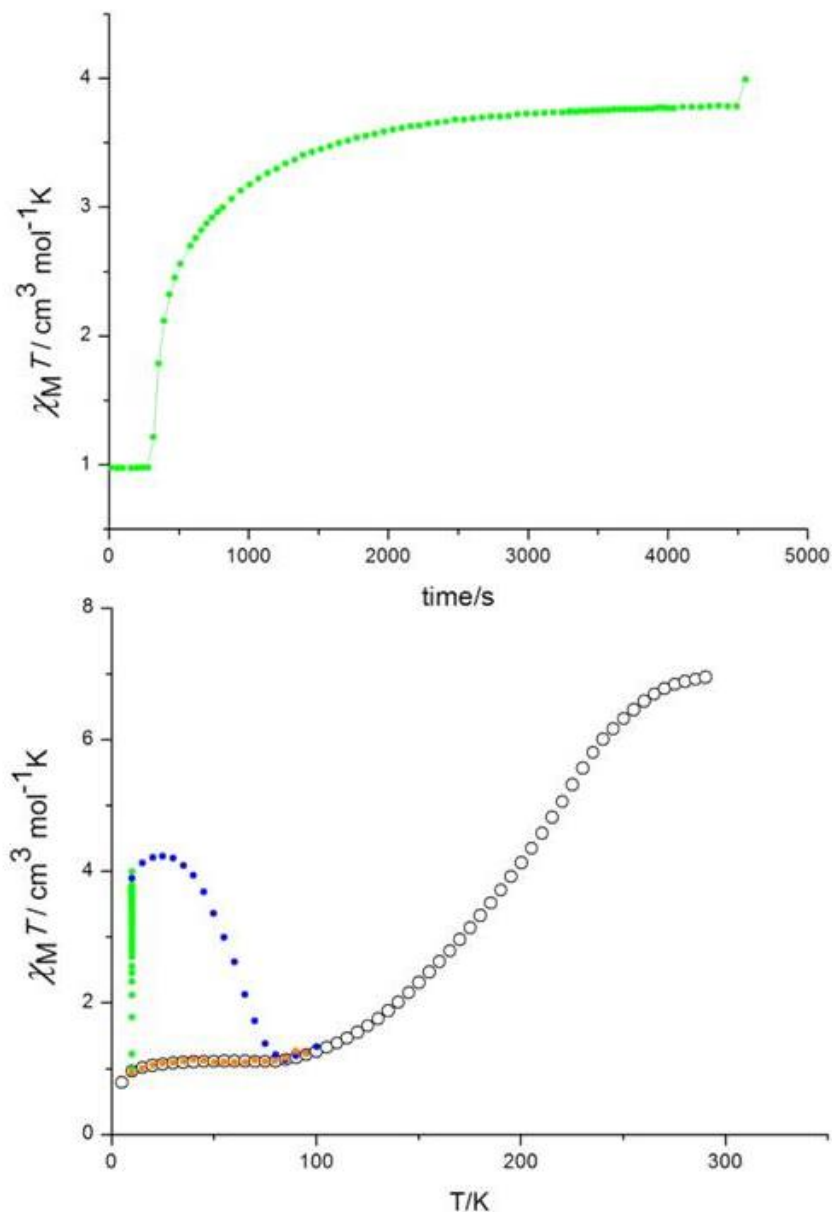
Figure 3.33: Top) time dependence of photo-induced $\chi_m T$ value ($\lambda = 500$-650 nm) of compound **2a**. Bottom) $\chi_m T$ *vs T* plot of LIESST effect experiment. Green circles represent measurements through irradiation of light. Blue circles represent the thermal dependence of $\chi_m T$ after switching off the light. Orange circles represent $\chi_m T$ values in cooling mode after complete relaxation. Open gray circles represent the bulk magnetic measurements before irradiation.

After switching off the irradiation and upon heating, the thermal dependence of $\chi_m T$ was recorded. The $\chi_m T$ value increases gradually from 3.20 $cm^3 mol^{-1} K$ at 10 K to reach a value of 3.20 $cm^3 mol^{-1} K$ at 25 K. Then, the $\chi_m T$ value decreased to the complete relaxation at 80 K. The T_{LIESST} value is around 60 K.

The $\chi_m T$ vs. T curve of a thin sample (0.2 mg) of **2a** before irradiation shows one-step SCO from [HS-HS] to [LS-LS] state (Figure 3.33). This behavior reveals slight difference to what observed in the bulk magnetic measurements shown in Figure 3.24. The main difference is the disappearance of the inflection point, which indicates the two-step SCO behavior. This can be explained by the higher content of water in the second sample as result of exposing to ambient environment for longer period. However, the HS residual seen in the second sample is around 15 %, which less than the one observed in the first bulk measurements (around 20%).

Irradiation of **2a** at 10 K, caused a rapid and efficient photo-induced conversion, saturating at 3.80 $cm^3 mol^{-1} K$ (Figure 3.33) after 1 hour of irradiation with 50 % of Fe(II) centers turning from LS to HS state. This behavior could be explained by the complete conversion from LS to HS of only one Fe(II) center of the helicate (i.e. [LS-LS] to [HS-LS] state). As discussed in **1a**, the photo induced state could correspond to Fe(II) center exhibiting SCO at lower temperature.

After switching off the light, the thermal dependence of $\chi_m T$ show a gradual increase reaching 4.24 $cm^3 mol^{-1} K$ at 25 K as a result of the magnetic anisotropy of the photo-induced HS state Fe(II) centers. Above 25 K, $\chi_m T$ value decreased due to thermal relaxation from HS to LS state where the relaxation is complete at 83 K and the T_{LIESST} value is around 65 K.

It was shown by investigation of large number of Fe(II) complexes that the empirical formula $(T_{LIESST} = T_0 + 0.3 T_{1/2})$[19] can be applied. T_0 depends on the denticity of the ligand. Applying this formula on the compounds **2**, **1a** and **2a** that exhibit clear LIESST effect gives T_0 values of 116, 122 and 121 K, respectively. These values agree with the data from the literature that shown that the three bidentate ligands show values around the straight line of T_0 value equal to 120 K.[28]

3.12 Solution Studies of the $X \subset Fe_2$ Helicates

To investigate the behavior of the $X \subset Fe_2$ Helicates in solution, ^{1}H NMR and ESI-MS measurements of crystals of **1** and **2** were conducted in acetonitrile. Compounds **3** and **4** are unstable in DMSO as indicated by ^{1}H NMR spectroscopy. Due to their very low solubility in other solvents, they were excluded from this study.

3.12.1 ^{1}H NMR Spectroscopy

The ^{1}H NMR spectrum of **1** is shown in Figure 3.34. The complex exhibits a dominant set of nine broad, paramagnetically shifted peaks (between –6 and 60 ppm) with no hyperfine splitting of which, two integrate for half the intensity of the other seven. Two of the latter resonances are degenerate near 40 ppm, but comparison with the Br^- analogue (see below) unveils the existence of two peaks in that area. These features are consistent with the idealized symmetry shown by the helicate of **1** in the solid state (D_3), suggesting that this is the major species in solution. The spectrum shows a smaller set of broad signals, spanning over a narrower range of chemical shifts (1 to 15 ppm). Their compared integrations are consistent with the ensemble arising from a multiple of sixteen protons. This is in agreement with a coordination complex with all identical H_2L4 ligands but featuring lower symmetry than the helical assembly. In fact one species exhibiting H_2L4 coordinated to only one Fe(II) with formula $[Fe(H_2L)_3]^{2+}$ can be isolated and characterized from this reaction system, which would explain this response. This strongly suggests that the minor species correspond to the dimerized helical structure $\{Cl \subset [Fe(H_2L4)_3]_2\}^{3+}$ which has been prepared and characterized in the solid state independently (compound **5**, chapter 4). Under this premise, comparison of total integration values indicates that the helicate in **1** and the dimerized mononuclear helicate coexist in approximately 1:0.6 proportions. This agrees with the mass spectrum of **1** (see below) and **5** (chapter 4), which show peaks corresponding to both assemblies when one of them dissolved in solution (see below).

The ^{1}H NMR spectrum of **2** (Figure 3.35) corroborates the observations made with its Cl^- analogue. The main differences are *i*) the set of peaks for the minor species is now much weaker (indicating now an approximate partition of 1:0.1), *ii*) the signal that was degenerate in **1** is now resolved in two peaks, *iii*) a resonance that in **1** was located in between the signals of residual MeOH has now moved under one of the solvent peaks, *iv*) the most paramagnetically shifted peaks of the helicate exhibit now significantly

larger chemical shifts (-9.36 to 72.91 ppm). This experiment confirms that the $\{Br \subset [Fe_2(H_2L)_3]\}^{3+}$ unit is stable in MeCN with clear dominance over the less symmetric species and that **2** in solution exhibits a larger fragment of Fe(II) centers in the HS state than **1** (consistent with the solid state behaviour) as indicated by much larger paramagnetic shifts.
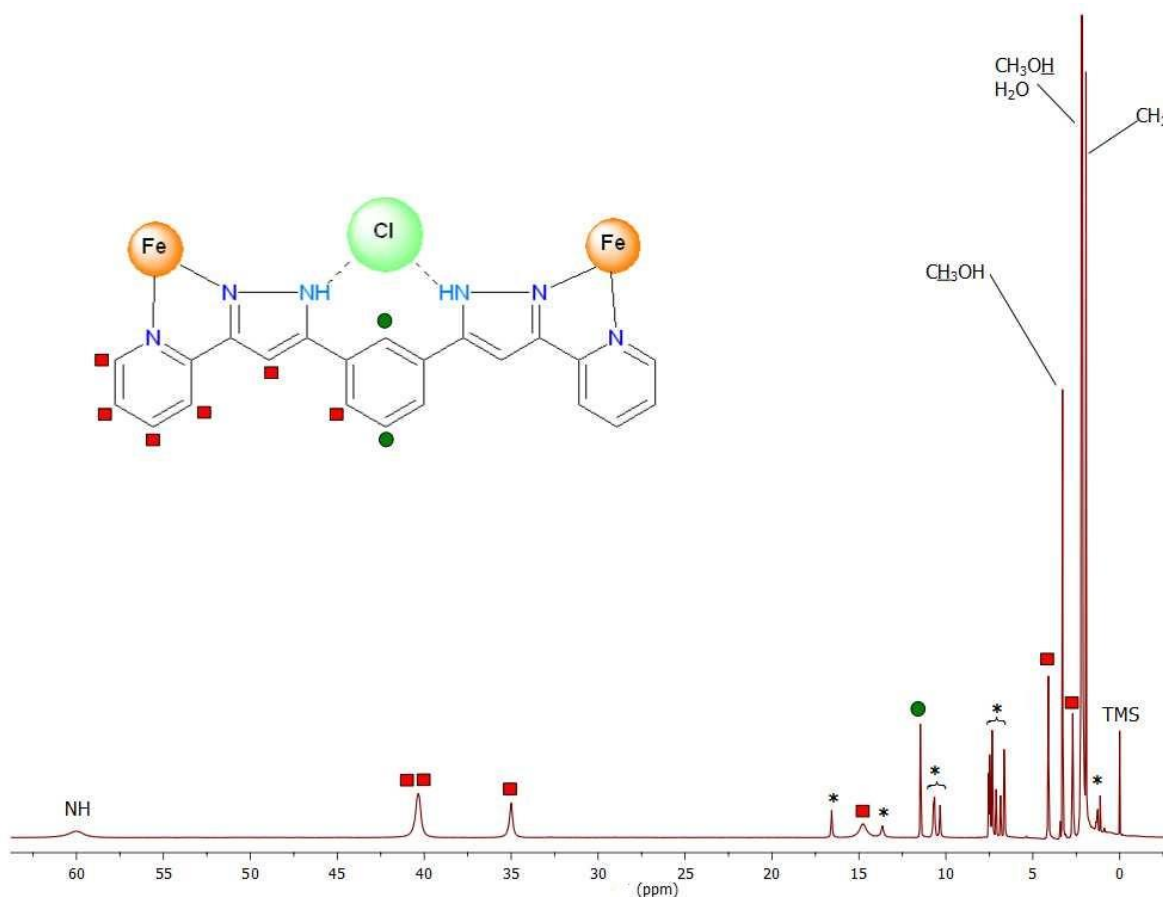
Figure 3.34: ^{1}H NMR of compound **1** in CD$_3$CN. Tentative assignment is shown for protons correspond to triple-stranded helicate. Peaks signed with stars correspond to minor specie mostly the dimerized helicate $\{Cl \subset [Fe(H_2L4)_3]_2\}^{3+}$ (see text for details).

The magnetic susceptibility for **1** and **2** in CD$_3$CN solution was measured at room temperature using modified Evan's method.[29,30] Using Wilmad-coaxial NMR tubes, solutions of **1** or **2** (3.43*10-3 and 1.33*10-3 mole/L, respectively) in CD$_3$CN containing 1% Me$_4$Si were placed in the main outer tube where as the insert tube was filled with same solvent (containing Me$_4$Si) as reference. ^{1}H NMR spectra were then recorded and two resonances for TMS were observed. These two peaks correspond to

TMS with or without the influence of paramagnetic species [HS Fe(II)]. The molar magnetic susceptibility is calculated according to the following equation:
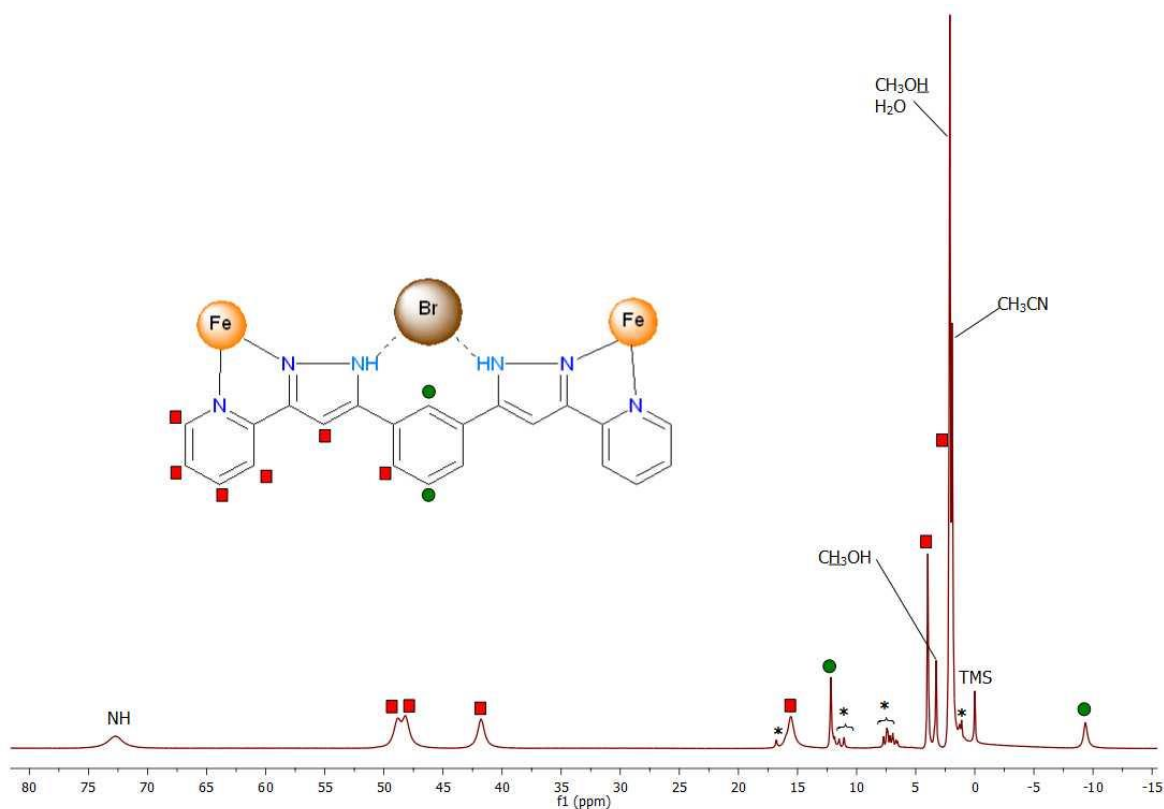
$$\chi_M = \frac{3000 * \Delta v}{4\pi v C} - \chi_M{}^{dia} \qquad (2)$$

Δv: is the difference in the chemical shift (Hz) of Me_4Si in the outer and the inner tubes.

v: is the spectrometer frequency in Hz.

C: is the concentration of the solution in mole/L.

$\chi_M{}^{dia}$: the diamagnetic contribution of the complex

Figure 3.35: 1H NMR of compound **2** in CD_3CN. Tentative assignment is shown for protons correspond to triple-stranded helicate. Peaks signed with stars correspond to minor specie mostly the dimerized helicate $\{Br \subset [Fe(H_2L4)_3]_2\}^{3+}$ (see text for details).

Applying this equation, $\chi_M T$ at room temperature for **1** and **2** were found to be 4.83 and 6.14 $cm^3 mole^{-1}K$, respectively. Using the obtained $\chi_M T$ value of the [HS-HS] state in the solid state, the $\chi_M T$ value in solution correspond to a total HS mole fraction (γ_{HS}) equal to 0.68 and 0.86 for **1** and **2**, respectively. The ratio of the observed γ_{HS} values for

compounds **1** and **2** $[\gamma_{HS}(Br)/\gamma_{HS}(Cl) = 1.27]$ is similar to the ratio observed in solid state at the same temperature. One must consider that the solution system consist of equilibrium between the $\{X \subset [Fe_2(H_2L4)_3]\}^{3+}$ helicate and the $\{X \subset [Fe(H_2L4)_3]_2\}^{3+}$ minor species. However, the minor species show mostly LS state in solution as indicated by the narrow paramagnetic isotropic shift of the corresponding peaks and the magnetic studies of these compounds as seen in chapter 4 which indicate the minor effect on the $\chi_M T$ calculated here. In any case, the high-low-spin population of the dinuclear helicate is influenced by the type of the anion in solution as in solid state. Accordingly, interacting with a stronger associated anion like Cl^- stabilizes LS state more than with Br^-. This result is in agreement with the result demonstrated by Barrett et al. for the $[Fe(3\text{-}bpp)_2]^{2+}$ system in solution. In the presence of hydrogen bonding anions, more strongly associated anions favor the LS state of the complex[15] (see section 3.9).

3.12.2 Mass Spectrometry

Mass spectrometry for compounds **1** and **2** were measured in CH_3CN using the positive ion electrospray (ESI^+) technique.

For compound **1**, the most prominent peaks were those representing free ligand (Figure 3.36). However, low intensity peaks with 2+ charge corresponding to the dinuclear triple-stranded helicate were observed in the region m/z = 500-650 (Figure 3.36). In particular, the peak of the anion-encapsulated-helicate $\{Cl \subset [Fe_2(H_2L4)_2(HL4)]\}^{2+}$ at m/z = 619.13 was detected, where one N-H unit have been deprotonated. The isotopic distribution of this peak is consistent with the theoretical one as shown in Figure 3.37. A peak correspond to free-of-anion triple stranded helicate $[Fe_2(H_2L4)(HL4)_2]^{2+}$ was also detected and confirmed by exact mass. These fragments confirm that the triple stranded assembly seen in the ^1H NMR spectrum is stable in CH_3CN solution.

Interestingly, another metal assembly is also observed in the ESI-MS spectrum corresponding to the dimerized helical structure. This assembly consists of two mononuclear triple stranded helicates held together by a central encapsulated Cl^- ion template (Chpater 4). Fragments of this assembly in the range m/z = 1100-1250 are seen in Figure 3.36. Peaks of these assembly were identified such as $\{Cl \subset [Fe(H_2L4)_3][Fe(H_2L4)_2(HL4)]\}^{2+}$ at m/z 1165.86 (Figure 3.37), $\{Cl \subset [Fe(H_2L4)_3]_2(PF_6)\}^{2+}$ at m/z 1239.36, $\{[Fe(H_2L4)_3][Fe(HL4)_3]\}^{2+}$ at m/z 1147.37 and

$\{[Fe(H_2L4)_3][Fe(H_2L4)_2(HL4)\ ](PF_6)\}^{2+}$ at m/z 1220.85. This confirms the coexistence of the dimerized helical structure and the triple stranded helicates seen in the ^{1}H NMR.
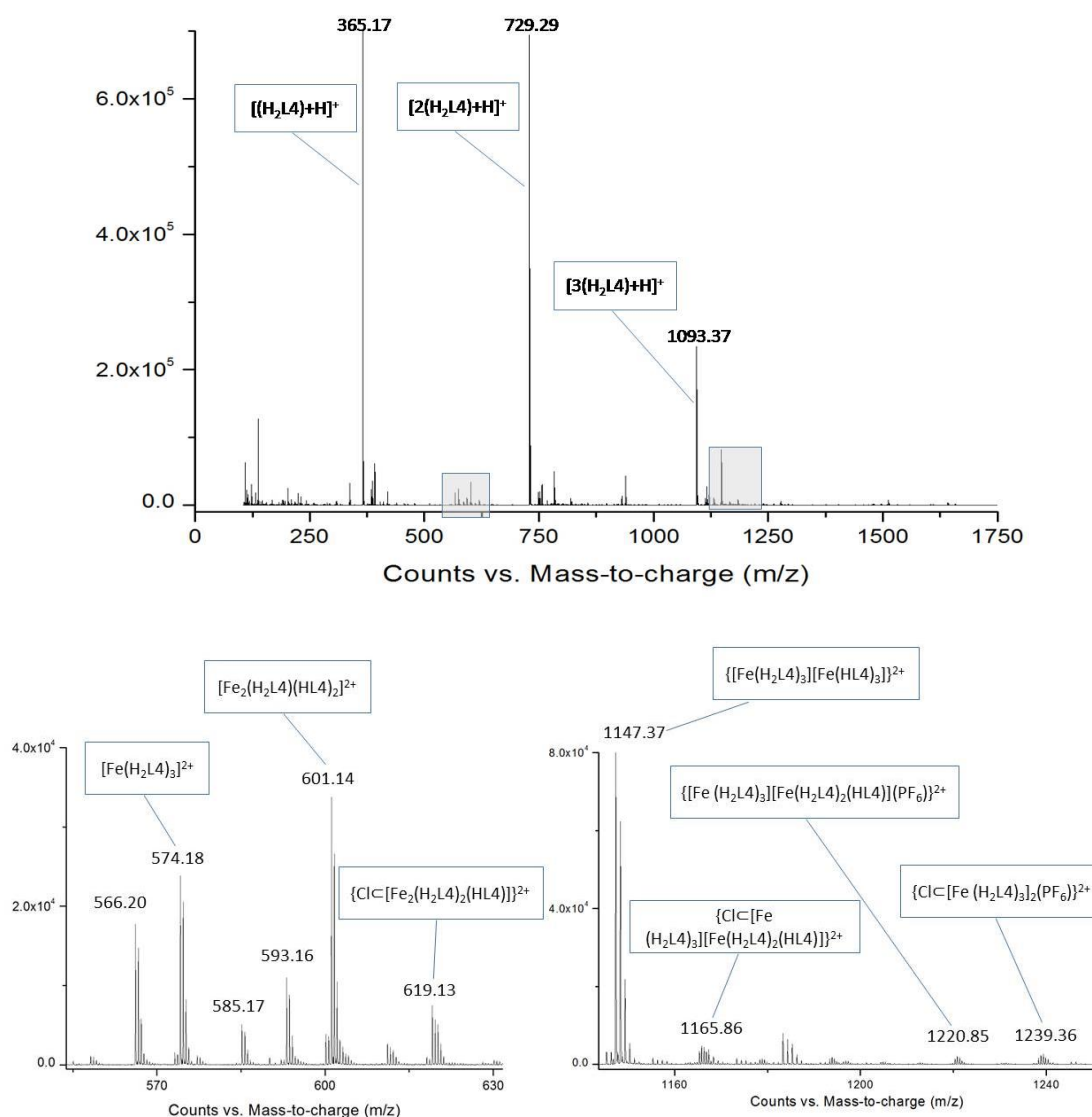
Figure 3.36: Mass spectrum of **1** in CH_3CN (top) and focusing on two regions (bottom). Peaks correspond to the dinuclear helicate and the dimerized helicate are assigned (see text for details).

In contrast, the mass spectra for **2** in CH_3CN revealed no peaks correspond to metal complexes in any significant amount. The Measurements show only peaks corresponding to the ligand (H_2L4). However, ^{1}H NMR study discussed before in the same solvent confirms the existence of the helical assembly in solution as in compound **1**. Consequently, **2** is fragile under the conditions of ESI-MS ionization or finds

difficulty to fly under the experimental set up which does not seem that they are not stable in solution.
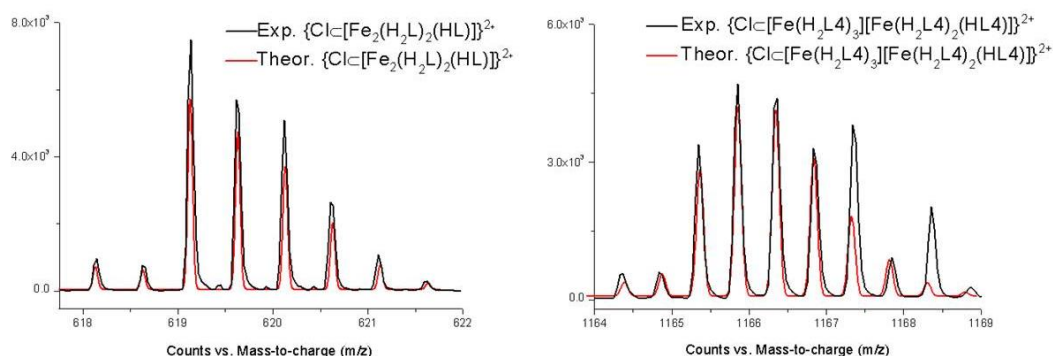
Figure 3.37: The match of theoretical and experimental isotopic distribution of {Cl⊂[Fe$_2$(H$_2$L4)$_2$(HL4)]}$^{2+}$ (left) and {Cl⊂[Fe(H$_2$L4)$_3$][Fe(H$_2$L4)$_2$(HL4)]}$^{2+}$ (right).

3.13 Conclusions

The ligand H$_2$L4 was successfully used to prepare a large number of dinuclear triple stranded helicates with an encapsulated halide (Cl$^-$ or Br$^-$) in their cavity using first row transition metals. X⊂[Fe$_2$(H$_2$L4)$_3$]$^{3+}$ helicates are a special case since they exhibit SCO properties. The spin state of the X⊂[Fe$_2$(H$_2$L4)$_3$]X(PF$_6$)$_2$ helicates can be tuned by changing the halide ions or the solvents in the lattice. MeOH solvate Fe$_2$ helicates exhibit half spin crossover conversion from [HS-LS] to [HS-HS] states. The LS state is more stabilized in the case of Cl⊂Fe$_2$ than for the Br⊂Fe$_2$ helicate, yielding a T$_{1/2}$ value around 30 K higher of the SCO.

Methanol solvent lattice exchange with the atmospheric H$_2$O via SCSC processes yielded a different SCO behavior in both cases. Two-step SCO from [HS-HS] to [LS-LS] states via intermediate [HS-LS] states are characteristic in the new water solvate helicates. Solvent exchange caused a disorder and displacement of the anions located around the metal ions in the lattice producing different interactions with these metals and thus causing different magnetic behavior. The spin transition temperature can be tuned also here with the different halide ions.

In contrast, [HS-HS] can be maintained over the temperature range 2-400 K in the X⊂[Fe$_2$(H$_2$L4)$_3$](I$_3$)$_3$ helicates. The counterions are now triiodide ions and they interact with

the helicate via lone pair-π interactions. The decrease of the number of hydrogen bonds interactions between the helicate and the counterions yielded this different magnetic behavior. $X \subset [Fe_2(H_2L4)_3]X(PF_6)_2$ helicates showed LIESST effect in both solvate cases. Metastable [HS-HS] and [LS-HS] states in methanol and water solvate helicates respectively can be photo-induced at low temperatures by irradiation with green light.

Solution studies of the $X \subset Fe_2$ helicates showed the stability of the triple stranded helicates in solution in equilibrium with another helical assembly. The second assembly consist of dimerized mononuclear helicate $\{X \subset [Fe(H_2L4)_3]_2\}^{3+}$ which also was isolated in solid state using different synthesis procedure (see Chapter 4).

3.14 Experimental

$Cl \subset [Fe_2(H_2L4)_3]Cl(PF_6)_2 \cdot 5.7CH_3OH$ (1). A suspension of H_2L (25 mg, 0.069 mmol) in methanol (10 mL) was added dropwise to a methanolic solution (5 mL) of $FeCl_2 \cdot 4H_2O$ (9.1 mg, 0.046 mmol). A red solution formed, which was stirred for 45 minutes, filtered and the filtrate treated with a methanolic (2 mL) solution of NBu_4PF_6 (14 mg, 0.036 mmol) and stirred for ten minutes. The resulting solution was layered with ether, which yielded red crystals after a few days. The yield was 17 mg (43 %). *Anal. Calc.* (Found) for **1**: C, 49.25 (49.18); H, 4.08 (4.24); N, 14.42 (14.30).ESI-MS: m/z 619.13 $\{Cl \subset [Fe_2(H_2L4)_2(HL4)]\}^{2+}$, m/z 601.14 $[Fe_2(H_2L4)(HL4)_2]^{2+}$

$Cl \subset [Fe_2(H_2L)_3]Cl(PF_6)_2 \cdot 3CH_3OH \cdot H_2O$ (1a). Crystals of **1a** were isolated by filtration and placed on a clean filter paper in the air for 5 days. The aged crystals were still suitable for single crystal X-ray diffraction. *Anal. Calc.* (Found) for **1a**: C, 48.81 (49.18); H, 3.80 (4.24); N, 14.85 (14.31).

$Br \subset [Fe_2(H_2L)_3]Br(PF_6)_2 \cdot 4CH_3OH$ (2). A suspension of H_2L4 (25 mg, 0.069 mmol) in methanol (10 mL) was added dropwise to a methanolic solution (5 mL) of $FeBr_2$ (9.9 mg, 0.046 mmol). A red solution formed, which was stirred for 45 minutes, filtered and the filtrate treated with a methanolic solution (2 mL) of NBu_4PF_6 (14 mg, 0.036 mmol) and stirred. The resulting solution was layered with ether, which yielded red crystals after a few days. The yield was 17 mg (41%). *Anal. Calc.* (Found) for **2**$\cdot$(+2H_2O): C, 46.22 (46.49); H, 3.76 (3.83); N, 13.86 (13.36).

$Br \subset [Fe_2(H_2L)_3]Cl \cdot (PF_6)_2 \cdot 1CH_3OH \cdot 1H_2O$ (2a). Crystals of **2** were isolated by filtration and placed on a clean filter paper in the air for 5 days. The aged crystals were

still suitable for single crystal X-ray diffraction. *Anal. Calc.* (Found) for **2a**·(+4.5H_2O): C, 44.73 (45.06); H, 3.75 (3.56); N, 13.75 (14.12).

Cl⊂[Fe$_2$(H$_2$L)$_3$](I$_3$)$_2$·3Et$_2$O (3). A suspension of H_2L (25 mg, 0.069 mmol) in methanol (10 mL) was added dropwise to a methanolic solution (5 mL) of $FeCl_2$·4H_2O (9.1 mg, 0.046 mmol). A red solution formed which was stirred for 30 minutes and filtered. The filtrate was treated with a methanolic solution (15 mL) of NBu_4I (40 mg, 0.108 mmol). The resulting solution layered with ether which yielded red crystals after ten days. The yield of crystals was 7.0 mg (11.5%).*Anal. Calc.* (Found) for **3**·0.5Et$_2$O: C, 36.36 (36.68); H, 3.17 (2.80); N, 9.54 (9.88).

Br⊂[Fe$_2$(H$_2$L)$_3$](I$_3$)$_2$·3Et$_2$O (4).A suspension of H_2L (25 mg, 0.069 mmol) in methanol (10 mL) was added dropwise to a methanolic solution (5 mL) of $FeBr_2$ (14.8 mg, 0.046 mmol). A red solution formed which was stirred for 30 minutes and filtered off. The filtrate was treated with a methanolic solution (15 mL) of NBu_4I (40 mg, 0.108 mmol). The resulting solution was layered with ether which yielded red crystals after ten days. The yield of crystals was 9 mg (14.3%). *Anal. Calc.* (Found) for **4**(–2.5Et$_2$O): C, 33.14 (33.02); H, 2.16 (2.08); N, 10.23 (10.16).

3.15 References

1   M. A. Halcrow, *Chem. Soc. Rev.*, 2011, **40**, 4119–4142.

2   S. Alvarez, *J. Am. Chem. Soc.*, 2003, **125**, 6795–6802.

3   A. Y. Verat, N. Ould-Moussa, E. Jeanneau, B. Le Guennic, A. Bousseksou, S. A. Borshch and G. S. Matouzenko, *Chem. - A Eur. J.*, 2009, **15**, 10070–10082.

4   A. L. Spek, *Acta Crystallogr. Sect. C, Struct. Chem.*, 2015, **71**, 9–18.

5   S. Mecozzi and J. Rebek, *Chem.-Eur. J.*, 1998, **4**, 1016–1022.

6   M. D. Pluth, D. W. Johnson, G. Szigethy, A. V. Davis, S. J. Teat, A. G. Oliver, R. G. Bergman and K. N. Raymond, *Inorg. Chem.*, 2009, **48**, 111–120.

7   S. Turega, M. Whitehead, B. R. Hall, M. F. Haddow, C. a. Hunter and M. D. Ward, *Chem. Commun.*, 2012, **48**, 2752.

8   J. Rebek, *Acc. Chem. Res.*, 2009, **42**, 1660–8.

9   R. D. Shannon, *Acta Crystallogr. Sect. A*, 1976, **32**, 751–767.

10   T. J. Mooibroek and P. Gamez, *CrystEngComm*, 2013, **15**, 1802.

11   G. Lemercier, N. Bréfuel, S. Shova, J. a. Wolny, F. Dahan, M. Verelst, H. Paulsen, A. X. Trautwein and J. P. Tuchagues, *Chem. - A Eur. J.*, 2006, **12**, 7421–7432.

12   M. Sorai, J. Ensling, K. M. Hasselbach and P. Gutlich, *Chem. Phys.*, 1977, **20**, 197–208.

13   Y. Garcia, P. J. van Koningsbruggen, René Lapouyade, L. Rabardel, O. Kahn, M. Wieczorek, R. Bronisz, Z. Ciunik and M. F. Rudolf, *Mol. Inorg. Chem.*, 1998, **1**, 523–532.

14   L. A. Sheludyakova and S. V Larionov, *Russ. J. Coord. Chem.*, 2003, **29**, 22–27.

15   S. A. Barrett and M. A. Halcrow, *RSC Adv.*, 2014, **4**, 11240.

16   Z. Ni and M. P. Shores, *J. Am. Chem. Soc.*, 2009, **131**, 32–33.

17   Z. Ni and M. P. Shores, *Inorg. Chem.*, 2010, **49**, 10727–35.

18   Z. Ni, A. M. McDaniel and M. P. Shores, *Chem. Sci.*, 2010, **1**, 615.

19   J.-F. Létard, *J. Mater. Chem.*, 2006, **16**, 2550.

20   J.-F. Létard, L. Capes, G. Chastanet, N. Moliner, S. Létard, J.-A. Real and O. Kahn, *Chem. Phys. Lett.*, 1999, **313**, 115–120.

21   R. J. Archer, C. S. Hawes, G. N. L. Jameson, V. McKee, B. Moubaraki, N. F. Chilton, K. S. Murray, W. Schmitt and P. E. Kruger, *Dalton Trans.*, 2011, **40**, 12368–73.

22   D. Pelleteret, R. Clerac, C. Mathoniere, E. Harte, W. Schmitt and P. E. Kruger, *Chem Commun*, 2009, 221–223.

23   M. Sorai, M. Nakano and Y. Miyazaki, *Chem. Rev.*, 2006, **106**, 976–1031.

24   Z. Arcis-Castíllo, S. Zheng, M. a. Siegler, O. Roubeau, S. Bedoui and S. Bonnet, *Chem. - A Eur. J.*, 2011, **17**, 14826–14836.

25   O. Roubeau, M. Castro, R. Burriel, J. G. Haasnoot and J. Reedijk, *J. Phys. Chem. B*, 2011, **115**, 3003–3012.

26   M. Sorai, *Top. Curr. Chem.*, 2004, **235**, 153–170.

27   T. Nakamoto, Z. C. Tan and M. Sorai, *Inorg. Chem.*, 2001, **40**, 3805–9.

28   J. F. Létard, C. Carbonera, J. A. Real, S. Kawata and S. Kaizaki, *Chem. - A Eur. J.*, 2009, **15**, 4146–4155.

29   D. H. Grant, *J. Chem. Educ.*, 1995, **72**, 39.

30   D. F. Evans, *J. Chem. Soc.*, 1959, 2003–2005.